Ecological Informatics 83 (2024) 102830

Contents lists available at ScienceDirect

Ecological Informatics

journal homepage: www.elsevier.com/locate/ecolinf

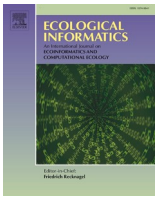

Reconstructing daytime and nighttime MODIS land surface temperature in desert areas using multi-channel singular spectrum analysis

Fahime Arabi Aliabad [a], Mohammad Zare [b], Hamidreza Ghafarian Malamiri [a], Amanehalsadat Pouriyeh [c], Himan Shahabi [d,e], Ebrahim Ghaderpour [f,*], Paolo Mazzanti [f]

[a] Department of Remote Sensing, Faculty of Geography, Yazd University, University Blvd., Safayieh, Yazd 8915818411, Iran
[b] Faculty of Natural Resources and Desert Studies, Yazd University, University Blvd., Safayieh, Yazd 8915818411, Iran
[c] Department of Environmental Science, Science and Research Branch, Islamic Azad University, Daneshgah Blvd, Simon Bulivar Blvd, Tehran 1477893855, Iran
[d] Division of Geochronology and Environmental Isotopes, Institute of Physics, Silesian University of Technology, Konarskiego 22B, Gliwicen 44-100, Poland
[e] Department of Geomorphology, Faculty of Natural Resources, University of Kurdistan, Sanandaj 6617715175, Iran
[f] Department of Earth Sciences & CERI Research Center, Sapienza University of Rome, P.le Aldo Moro, 5, Rome 00185, Italy

ARTICLE INFO

Keywords:
Cloud
Gap–filling
Hot and dry climate
Land surface temperature
Multi–channel singular spectrum analysis

ABSTRACT

The availability of continuous spatiotemporal land surface temperature (LST) with high resolution is critical for many disciplines including hydrology, meteorology, ecology, and geology. Like other remote sensing data, satellite–based LST is also encountered with the cloud issue. In this research, over 5000 daytime and nighttime MODIS–LST images are utilized during 2014–2020 for Yazd–Ardakan plain in Yazd, Iran. The multi–channel singular spectrum analysis (MSSA) model is employed to reconstruct missing values due to dusts, clouds, and sensor defect. The selection of eigenvalues is based on the Monte Carlo test and the spectral analysis of eigenvalues. It is found that enlarging the window size has no effect on the number of significant components of the signal which account for the most variance of the data. However, data variance changes for all the three components. Employing two images per day, window sizes 60, 180, 360, and 720 are examined for reconstructing one year LST, where these selections are based on monthly, seasonal, semi-annual, and annual LST cycles, respectively. The results show that window size 60 had the least computational cost and the highest accuracy with RMSE (root mean square error) of 2.6 °C for the entire study region and 1.4 °C for a selected pixel. The gap–filling performance of MSSA is also compared with the one by the harmonic analysis of time series (HANTS) model, showing the superiority of MSSA with an improved RMSE of about 2.7 °C for the study region. In addition, daytime and nighttime LST series for different land covers are compared. Lastly, the maximum, minimum, and average LST for each day and night as well as average and standard deviation of LST images in the seven-year-long time series are also computed.

1. Introduction

Land surface temperature (LST) is a crucial climate system variable used for various purposes, including climate, environmental, and natural hazard studies (Arabi Aliabad et al., 2023a; Ghaderpour et al., 2023; Hu et al., 2024; Xing et al., 2021). Meteorological stations lack an adequate spatial coverage to provide a reliable temperature estimate for their surrounding areas (Ahmed et al., 2023; Metz et al., 2017). Due to several factors, such as variations in solar radiation, atmospheric conditions, and land surface characteristics in space and time, LST changes both spatially and temporally (Li et al., 2018). The LST estimated using satellite images can capture in more detail the local temperature differences (Almeida et al., 2022; Arabi Aliabad et al., 2023b; Hengl et al., 2012).

The availability of spatially and temporally continuous LST time series with high resolution is critical for a wide range of disciplines including hydrology, ecology, and geology as well as numerous application fields and studies concerning sandstorms and desertification (Ghaderpour et al., 2024; Piao et al., 2023; Shawky et al., 2023; Weng, 2009; Zhu et al., 2013). LST can be utilized to retrieve relevant climate variables, such as soil moisture, evapotranspiration, thermal inertia, and water-stress vegetation (Agam et al., 2008; Aliabad et al., 2022; Kustas

* Corresponding author.
E-mail addresses: fahimearabi@stu.yazd.ac.ir (F.A. Aliabad), mzernani@yazd.ac.ir (M. Zare), hrghafarian@yazd.ac.ir (H.G. Malamiri), a.pouriyeh@srbiau.ac.ir (A. Pouriyeh), himan.shahabi@polsl.pl (H. Shahabi), ebrahim.ghaderpour@uniroma1.it (E. Ghaderpour), paolo.mazzanti@uniroma1.it (P. Mazzanti).

https://doi.org/10.1016/j.ecoinf.2024.102830
Received 4 June 2024; Received in revised form 17 September 2024; Accepted 20 September 2024
Available online 24 September 2024

and Anderson, 2009). Its application is vast, being effective in urban heat island (UHI) research (Almeida et al., 2021; Dousset and Gourmelon, 2003), cryosphere melting (Schneider and Hook, 2010), global warming studies (Hall et al., 2012), insect infestation (Pasotti et al., 2006), vector-borne diseases (Neteler et al., 2011), etc.

However, like other remote sensing data, LST faces the cloud problem (Ahmed et al., 2023). For example, the presence of data gaps created by cloud cover or the presence of outliers in pixels prevents the use and any subsequent interpretation of these images (Metz et al., 2014). Time series of satellite images usually have missing data and contain noise and outliers, due to cloud, aerosol, and algorithm malfunction that cause irregular observations (Ahmed et al., 2023; Pan et al., 2024). About 68 % of the Earth surface is covered by clouds every day on average, limiting LST applications (Li et al., 2023; Stubenrauch et al., 2013). Many attempts have been performed to properly mask clouds from remote sensing satellite imagery (Ahmed et al., 2023; Simpson and Gobat, 1996; Stowe et al., 1991; Taheri Dehkordi et al., 2022). Having regularly sampled time series need gap–filling, determining outliers and removing them from the original time series.

Many models dealing with gap–filling and removing outliers from time series are proposed in the past decades (Ahmed et al., 2023; Fang et al., 2007; Julien et al., 2006; Kondrashov et al., 2010; Moffat et al., 2007). The LST gap–filling models can be divided into five groups: (1) temporal gap–filling based on temporal information from each pixel, i.e., these models are based on per–pixel LST time series (Arabi Aliabad et al., 2024; Zhou et al., 2021), (2) spatial gap–filling based on information of adjacent pixels, i.e., these models are image–based, such as Kriging (Siabi et al., 2022; Zhang et al., 2007), (3) spatiotemporal reconstruction methods, where LST information of the neighboring pixels is considered both in space and time (Yan et al., 2023; Yao et al., 2021; Zhang et al., 2020), (4) multi-fusion methods (Duan et al., 2017; Mo et al., 2023), and (5) gap–filling methods based on surface energy balance (Jia et al., 2021; Mo et al., 2023; Song et al., 2023). Each of these models has its own advantages and limitations, summarized in Table 1.

Temporal models rely on the information content that may exist in time series, e.g., trends and periodic cycles. Such models work well when gaps are not too long and continuous, and so the harmonic components can be well approximated by methods, such as Fourier and wavelet analyses (Ahmed et al., 2023; Ghaderpour et al., 2023). Xiao et al. (2021) proposed a random forest regression technique to fill the gaps in LST time series in Chongqing City, reaching $R^2 = 0.89$. Although machine learning models have good performance accuracy, their results are limited by the quality of the training datasets (Tian and Zhang, 2022). Moreover, it is also hard to find appropriate auxiliary spatial parameters with fine resolution given the complex formation of the dependent variables (Buo et al., 2021; Sarafanov et al., 2020).

As one among various temporal models, annual temperature cycle (ATC) models enable a continuous description of the LST cycle on an annual scale (Fu and Weng, 2018). Zhu et al. (2022) showed that the root mean square error (RMSE) using an ATC model is between 0.9 and 2.5 K. However, the prediction accuracy of the ATC models in literature is usually low because of their limited parameters and ignoring spatial information (Fu et al., 2022; Liu et al., 2019). In areas where daily and seasonal temperature changes are extreme, such as arid regions, ATC models may not be able to respond well to these rapid and extreme changes and provide inaccurate estimates for the missing LST values. The ATC models are based on some simplifying assumptions which may not be true in all situations.

The harmonic analysis of time series (HANTS) is another temporal model that is based on a series of sinusoidal (harmonic) functions (Xu and Shen, 2013). Models with relatively more sophisticated forms have a higher accuracy, but their generalization abilities are relatively low due to the large number of parameters (Zhou et al., 2023). A limitation of HANTS is that only the temporal correlation between observations is used to fill the gap in LST images (Zhou et al., 2021).

The singular spectrum analysis (SSA) is a robust time series analysis model that uses multivariate statistical analysis, linear algebra, and signal processing (Broomhead and King, 1986; Golyandina and Zhigljavsky, 2013). The SSA is primarily a data matching technique which decomposes a time series into meaningful components, such as trend, periodic and quasi-periodic, and noise. In practice, several significant components form most data variance (signals), while others are usually referred to noise. One of the main concepts of SSA is how components can be separated from one another (Golyandina et al., 2001). The multi–channel SSA (MSSA), a robust extension of SSA, considers the temporal and spatial correlations between multiple time series simultaneously (Ghil et al., 2002; Weinberg and Petersen, 2021).

In a dynamic Earth system, LST variation over time can be due to several factors, such as land cover change variation and tilted spin axis of the Earth and its motion around itself and the Sun (Ghaderpour et al., 2023). Therefore, LST change over time often contain periodic and aperiodic/irregular components. Using this theory, SSA uses empirical orthogonal functions (EOFs) and principal component analysis (PCA) to directly separate signal from noisy time series without any prior knowledge about their nature (Vautard and Ghil, 1989). The trend and structure of a time series in a defined time interval, e.g., in a window size, can be considered as the sum of several simple and elementary processes, such as trend, significant fluctuations and noise. The main goal of PCA is to transform a set of dependent variables into another set of independent variables that is smaller, so that the first few components form the most data variance (Jolliffe, 1990). The methodological aspects and applications of SSA and MSSA have attracted the attention of many researchers (Vautard et al., 2013; Yiou et al., 2000). These models proved to be robust in various applications and have recently become standard tools for climate and geoscience studies.

Seitola et al. (2015) carried out random MSSA of climate data and showed that a 2–6 year variability concentrated in the pacific ocean has been taken by all datasets with differences in statistical significance and spatial patterns. Ghafarian Malamiri et al. (2018) filled the gaps of LST time series products using SSA and estimated a RMSE of 2.95 K between the reconstructed and original LST time series data in their study region. Their findings showed that SSA using spatiotemporal interpolation can effectively be used to solve the cloud contamination issue resulting in missing data. Ghafarian Malamiri et al. (2020) utilized HANTS and MSSA for reconstructing normalized difference vegetation index (NDVI) images of Landsat with a 16-day sequence and showed that MSSA is a suitable method for solving the challenge of missing data in vegetation time series.

Selecting the best gap–filling model depends on the specific conditions of the study. In studies where rapid temporal changes are more important, temporal models are more appropriate. While in studies where spatial variation is paramount, spatial models are suitable. Spatiotemporal methods can reconstruct LST images with a higher

Table 1
A summary of gap–filling models with their advantages and shortcomings.

Models	Advantages	Shortcomings
Temporal	Simplicity, high speed, suitable for data with fast temporal changes	Not considering spatial changes, sensitivity to noise and strong spatial changes
Spatial	Consideration of spatial changes, suitable for data with gradual spatial changes	The need for high-quality spatial data, sensitivity to rapid temporal changes
Spatiotemporal	Considering both temporal and spatial changes, high accuracy in reconstruction	High computational complexity, need for high quality data
Multi-fusion	High flexibility, ability to adapt to different data conditions	Complexity of choosing and combining methods, the need to adjust multiple parameters
Based on surface energy balance	Strong physical base, high accuracy in certain conditions	The need for large input data, high computational complexity

accuracy, especially when LST significantly changes both temporally and spatially. In Yazd-Ardakan plain, since LST varies significantly in time and space due to high desert conditions, MSSA, a robust spatio-temporal model, is applied to reconstruct LST images. The main contributions of the present research are as follows.

- Reconstructing daytime and nighttime MODIS-LST images for the study region via MSSA by finding the most optimal window size.
- Comparing MSSA with HANTS using RMSE to show the advantage of MSSA over HANTS for reconstructing LST images.
- Investigating the relationships between land cover/use classes and LST within the study region in a one-year period.

In addition, for each daytime and nighttime LST image, the maximum, minimum, and average values of the LST image are estimated from the LST values between the 2nd and 98th percentiles of the LST image, reducing the effect of potential outliers. Then the LST time series for period 2014–2020 for the study region are illustrated. The daily and nightly averages and standard deviations of the reconstructed LST images for the study region are also illustrated. The present study, unlike most studies that use a one-year time series to reconstruct LST images, a seven-year time series is chosen for gap–filling of MODIS images as mentioned in the literature review.

The results of this research are practical and useful for studies that are based on the complete time series of LST in day and night in monitoring temperature changes, geothermal, land cover change monitoring, and others. In the remaining of the present article, the study region, datasets, mathematical details of MSSA, and gap–filling results are demonstrated, and a comparison is made between HANTS and MSSA by calculating their RMSEs. The LST variation for different land use/cover classes in a one-year period and LST time series for the seven-year-long period are illustrated as well as maps of averages and standard deviations of the reconstructed LST images. In addition, a comprehensive discussion is given on the advantages and limitations of gap-filling models and implications of complete LST image time series in environmental monitoring and ecosystems.

2. Materials and methods

2.1. Study region

The Yazd–Ardakan plain has an area of more than 1,174,000 ha, located in the southwest of Yazd province. This region is limited to the heights of Siyakouh, Shirkouh, and Kharanaq. It has a long-term annual average rainfall of 60 mm and has a hot and dry climate (Pouriyeh et al., 2021). Fig. 1 displays the study region located in Yazd-Ardakan, Yazd, Iran. The main part of the region is covered by rangelands which include lowland plains with very poor vegetation. Due to low amount of rainfall, the life span of vegetation which mainly grows in spring is very short. The second largest area is covered by mountainous lands which are poor in terms of vegetation. The study region is also covered by sand dunes and bare lands with almost no vegetation cover. In addition, a small part of the study region is residential and agricultural lands. For the purposes of visualization, validation, and showing the performance of different window sizes in MSSA for LST reconstruction, one pixel is selected as an example that does not have significant missing data during the seven-year period and is near a weather station, shown by a star in Fig. 1d. The land cover map is produced by the authors for a general understanding of the study region. This map was prepared using Sentinel 2 images from the summer of 2020, with a spatial resolution of 10 m and

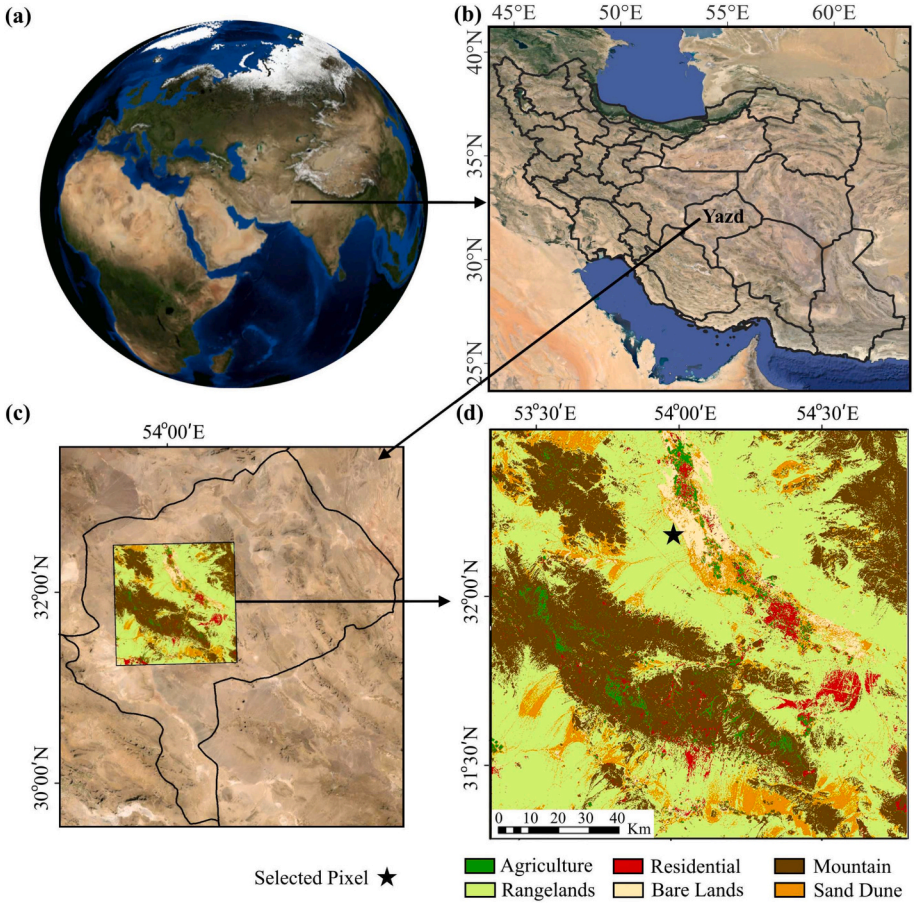

Fig. 1. Study region: (a) the location of Iran in the world, (b) Iran, (c) Yazd province, and (d) the land cover map of the study region.

using the maximum likelihood algorithm (Phiri et al., 2020).

2.2. Datasets

The estimation of LST image using satellite images started in 1970 (McMillin, 1975). Numerous satellite LST products have been developed from a variety of sensors (Chander et al., 2009; Jiang and Li, 2008). The MODIS–LST imagery have been widely utilized in many studies for climate and environmental monitoring (Ahmed et al., 2023; Ghaderpour et al., 2023; Shawky et al., 2023; Song et al., 2021). The MODIS product with a spatial resolution of 1 km and repeating 4 times a day has widely been used (Xian et al., 2021; Yoo et al., 2018). The split window algorithm is used to estimate the temperature product of the MODIS (Wan and Dozier, 1996). The accuracy of MODIS–LST products is between 1 and 2 Kelvin (Duan et al., 2019; Tan et al., 2021). Unfortunately, MODIS or other thermal infrared (TIR)–based LSTs are sensitive to clouds and atmospheric noise and so cannot produce reliable results in regions with high humidity due to rainfalls (Cho et al., 2020, 2022; Ghaderpour et al., 2023). In this research, the daily and nightly MODIS–LST products are employed for every day of the year over the period of 2014–2020 which includes 5114 images – MOD11A1 (Duan et al., 2019; Li et al., 2021) provided by National Aeronautics and Space Administration (NASA): https://modis.gsfc.nasa.gov/data/dataprod/mod11.php (Last accessed on Sep 1, 2023).

2.3. Multi–Channel singular Spectrum analysis (MSSA)

The MSSA is an extension of SSA used when there is more than one time series, e.g., time series of daily LST maps (Broomhead and King, 1986; Rodrigues and Mahmoudvand, 2018). The SSA is a linear model for processing and predicting the behavior of a time series. The SSA is a non-parametric model (adaptive to the data), and so it has advantage over classical Fourier analysis. Fourier analysis is a model-based method that can effectively process stationary and periodic time series. However, when the time series contains many periodic/aperiodic components, it requires many frequencies for time series reconstruction. In Fourier analysis, harmonic functions are estimated while elementary components are estimated in SSA. Thus, if the time series has intrinsic components, SSA will also be periodic. Due to its data adaptivity nature, SSA can process nonlinear dynamics without any underlying assumptions about the data. The main aim of SSA is spectral division. There are two types of matrix simplification, elimination for solving linear systems and spectral decomposition. The SSA has four steps that are briefly described below.

Step 1. A time series $f_1, f_2, \ldots, f_n$ is converted to a multidimensional trajectory matrix containing lagged vectors as follows.

$$\mathbf{X} = \begin{bmatrix} f_1 & f_2 & \cdots & f_\kappa \\ f_2 & f_3 & \cdots & f_{\kappa+1} \\ \vdots & \vdots & \vdots & \vdots \\ f_m & f_{m+1} & \cdots & f_n \end{bmatrix} \tag{1}$$

where m ($m < n$) is the window size, n is the size of a time series and $\kappa = n - m + 1$. Matrix $\mathbf{X}$ contains the complete records of patterns in the window. Large window sizes result in expanding spectral domain of SSA and processing more data for recognizing initial time series pattern. However, reducing the window size expands the statistical confidence as the time series structure is considered continuously (Elsner and Tsonis, 1996).

Step 2. Decompose $\mathbf{X}$ using the singular value decomposition (SVD):

$$\mathbf{X} = \mathbf{DLE}^{\mathrm{T}} \tag{2}$$

where T is transpose, $\mathbf{D}$ is the left and $\mathbf{E}$ is the right singular vectors of the matrix $\mathbf{X}$ with dimensions $m \times m$ and $\kappa \times \kappa$, and $\mathbf{L}$ is the rectangular diagonal matrix with dimensions $m \times \kappa$. The entries of $\mathbf{L}$ are the square roots of the eigenvalues of the lagged-covariance matrix $\mathbf{S} = \mathbf{X}^{\mathrm{T}}\mathbf{X}$ with dimension $m \times m$. Matrix $\mathbf{S}$ is symmetric and its entries are proportional to correlation between snapshots pairs. The columns of matrix $\mathbf{D}$ are input features of $\mathbf{S}$ or empirical orthogonal functions (EOFs). The rows of the $\mathbf{E}^{\mathrm{T}}$ matrix are the eigenvectors of $\mathbf{S}$. For a periodic time series whose corresponding eigenvalues contain large covariance values toward the diagonal entries of posterior-covariance matrix, their periodic components reflect the eigenvectors. Parts of periodic patterns can appear in phase and other parts can be outside the phase. Entries with high covariance along the diameter of the lagged-covariance matrix $\mathbf{S}$ show variations in the time series. If the unique values are plotted in descending order, it is often possible to separate a steep initial slope (signal) and a flat level (noise). Then, each subset of d eigenvectors, $1 \le d \le m$, (EOFs) such that their corresponding eigenvalues are positive, gives best representation of matrix $\mathbf{X}$ as $\mathbf{X} = \mathbf{X}_1 + \cdots + \mathbf{X}_d$.

Step 3. Partition the elementary matrices $\mathbf{X}_j$ ($j = 1, \ldots, d$) into p disjoint subsets and summing the matrices within each subset. More precisely, let $I_\ell = \{\ell_1, \ell_2, \ldots, \ell_p\}$ be a group of indices belonged to $\{1, 2, \ldots, d\}$, where $1 \le \ell \le m$. Then

$$\mathbf{X} = \mathbf{X}_{I_1} + \mathbf{X}_{I_2} \cdots + \mathbf{X}_{I_m}, \tag{3}$$

where $\mathbf{X}_{I_\ell} = \sum_{k \in I_\ell} \mathbf{X}_k$ for $\ell = 1, 2, \ldots, m$. The process of choosing the sets $I_1, \ldots, I_m$ is known as the eigentriple grouping. Matrices $\mathbf{X}_{I_\ell}$ are ideally in a Hankel matrix form, and thus they can fit the trajectory matrices (Ghafarian et al., 2012).

Step 4. The $\mathbf{X}_{I_\ell}$ matrices must be transformed into a Hankel matrix form if they are not already to be aligned with the trajectory matrices (diagonal averaging). Therefore, adding these matrices can produce the original matrix.

$$\mathbf{X} = \mathbf{Y}_{I_1} + \mathbf{Y}_{I_2} \cdots + \mathbf{Y}_{I_m}, \tag{4}$$

where $\mathbf{Y}_{I_\ell} = H\mathbf{X}_{I_\ell}$ is Hankelization of a matrix $\mathbf{X}_{I_\ell}$ for $\ell = 1, 2, \ldots, m$.

The MSSA uses M number of spatiotemporal profiles ($M \le m$), where m is the size of the selected window in SSA and spatial data. An optimal number of significant components (S–PCA) of the spatial time series along with temporal data (T–PCA) is used for more accurate reconstruction of time series, especially the parts with long missing data. If there are M time series, then the multivariate covariance matrix $\mathbf{C}$ as an important step of MSSA can be produced as follows.

$$\mathbf{C} = \begin{bmatrix} \mathbf{C}_{1,1} & \mathbf{C}_{1,2} & \cdots & \mathbf{C}_{1,M} \\ \mathbf{C}_{2,1} & \mathbf{C}_{2,2} & \cdots & \mathbf{C}_{2,M} \\ \vdots & \vdots & \vdots & \vdots \\ \mathbf{C}_{M,1} & \mathbf{C}_{M,2} & \cdots & \mathbf{C}_{M,M} \end{bmatrix} \tag{5}$$

where $\mathbf{C}_{i,j}$ is the multivariate covariance matrix of order κ between channels i and j like matrix $\mathbf{S}$ for SSA with one univariate time series (Weinberg and Petersen, 2021). This covariance matrix simultaneously autocorrelates individual time series and cross-correlates different time series, accounting for significance of spatiotemporal information of multiple time series. The rest of the process is like SSA, noting that each eigenvector has a block of length κ, one block for each time series.

The SSA considers segments of a single pixel time series while MSSA considers segments of multiple pixels time series simultaneously. In other words, each submatrix $\mathbf{C}_{i,j}$ in covariance matrix $\mathbf{C}$ has the same dimension as in the one-dimensional SSA; however, $\mathbf{C}$ simultaneously auto-correlates both individual time series like in SSA and cross auto-correlates different rime series. Hence, $\mathbf{C}$ considers the common temporal information that is significant among different time series within a spatial window, especially useful for a more accurate estimation of missing values when there exist long temporal gaps in spatial time series as compared to temporal based models like HANTS. Further details about MSSA can be found in Ghil et al. (2002); Weinberg and Petersen (2021).

2.4. Monte Carlo singular Spectrum analysis

Auto-correlated noise (red noise) is serially correlated in time, i.e., two successive observations have lag-one autocorrelation:

$$x_t = ax_{t-1} + \epsilon_t, \tag{6}$$

where x_t is an observation at time t, x_{t-1} is a modified copy of the same variable at time $t-1$, lag-one is the covariance between x_t and x_{t-1}, ϵ_t is a random error (white noise) whose mean is zero and has a standard deviation of σ that along with a are the process parameters (Ghafarian Malamiri, 2015). Allen (1992) proposed Monte Carlo SSA to detect signal from noise. The red noise hypothesis will be accepted in many cases. To define a red noise, the parameters σ and a which describe it need to be estimated. The red noise value at time t is dependent on the value at time $t-1$, and the parameters can be estimated from the time series itself. If one selects a set of parameters that results in rejecting of the red noise null hypothesis, while another set of parameters result in accepting the null hypothesis, then the decision will be indecisive. Allen (1992) estimated unbiased red noise parameters utilizing maximum likelihood criteria. The easiest way to compute the red noise parameters is using the time series lag-one auto-covariance a and standard deviation σ. Given the red noise parameters, different realizations of the red noise can be created considering an initial value (x_0) and different white noise sets. The idea is that if one takes various realizations of the red noise, the same expected variance and lag-one covariance are expected as those of the time series itself.

Thus, in this case, there are P sets of alternative time series, each has the same values. For each surrogate (surr), $\mathbf{S}^{\text{surr}}$ and its eigenvalues λ^{surr} are computed by

$$\lambda^{\text{surr}} = \mathbf{E}^{\text{surrT}}\mathbf{S}^{\text{surr}}\mathbf{E}^{\text{surr}}. \tag{7}$$

Then, a set of P values for each state is utilized to form a distribution function according to the percentage of significance levels that can be computed. By plotting the eigenvalues, statistically significant eigenvalues and its corresponding eigenvectors can be determined (e.g., at 95 % confidence level). If the eigenvalue is higher than the percentage λ^{surr}, it can be deduced that this eigenvalue is statistically significant, and so the noise null hypothesis of noise is not accepted. This mode is associated with a specific signal with its corresponding frequency and period (Ghafarian Malamiri, 2015).

2.5. Time series reconstruction

The MSSA process to fill missing data and outliers includes several steps. For a window size m, first calculate the average values of the time series to centralize the time series and set the missing data to zero. The first EOF of the index is found by an iterative process, which runs MSSA on the zero-centered data. Then update the missing values according to the reconstructed components of the current EOF derived by displaying the EOF on the original time series. The MSSA is used again on this updated set so that the EOF is computed twice, and the missing values are filled. This process is repeated until the convergence test is satisfactory. The normalized RMSE (as a benchmark) is computed between the new reconstructed data and the missing data from the former iteration till the difference between two consecutive normalized RMSE values becomes less than 2.5 % (Gupta and Ramani, 1980). Iteration is then started for the second prominent EOF (holding the first constant) until convergence is achieved for the second EOF. For the selected number of EOFs, this process continues while the previous parameters are kept constant each time. Cross-validation is used to determine an optimal window size and SSA modes for time series reconstruction. A part of the available data, chosen randomly, is converted to missing data, and the reconstruction RMSE is computed to determine the optimal value for the window size and number of EOFs. The general formula for RMSE is given by

$$\text{RMSE} = \sqrt{\frac{1}{n}\sum_{i=1}^{n}(y_i - \hat{y}_i)^2}, \tag{8}$$

where n is the size of time series, y_i are time series values (true) and $\hat{y}_i$ are the estimated values (predicted). Considering that RMSE is proportional to the measurement unit of the variable, one may not use it directly for comparing the performance of models built for variables with different units. The normalized RMSE is calculated by dividing the value of RMSE into the range of data of the dependent variable, suitable for comparing different models. Generally, the normalized RMSE below 10 % indicates good accuracy of the model, 10–20 % indicates the model is appropriate, 20–30 % indicates an average accuracy, and more than 30 % indicates that the model is weak. There exists no straightforward way in MSSA to remove outliers, but as few principal components are employed in the reconstruction, the outliers are removed indirectly in the final normalized signal. However, outliers still affect the reconstruction. The overall workflow of this work is summarized in Fig. 2.

3. Results

In this section, the ability of MSSA to fill in the missing data of the image and remove and correct outliers under the presence of noise is discussed. Then MSSA validation is carried out using original and reconstructed data. It is shown how to select an optimal window size, the number of main components of MSSA, and the number of eigenvalues by eigenvalue spectrum analysis and the Monte Carlo test.

3.1. An optimal window size for reconstructing MODIS–LST images

From Monte Carlo examination and eigenvalues spectrum analysis, a number of eigenvalues is chosen, covering most part of the eigenvalue spectrum. If the eigenvalues of a time series are plotted in descending order, the resulting graph shows two different slopes. At the beginning of the graph, a steep slope is created, which indicates the significant components of the signal. After that there is a smooth trail with a low slope that represents signal noise.

Fig. 3a shows the spectrum of eigenvalues corresponding to the selected pixel in the seven-year-long time series of the MODIS–LST with the sequence of day and night with a window size 60 (one month) as a representative of the data. According to Fig. 3a, the three main components are located in the steep part of the graph, which are the significant components of the signal and account for the largest amount of data variance. At the beginning of the graph, there is an initial steep slope, which shows the significant components of the signal, after this sequence of the graph, there is a low and relatively smooth slope, representing noise. Fig. 3b presents the temporal EOFs of the significant components in this time series according to the results of the Monte Carlo test. Component 1 (in blue) in Fig. 3b shows the same day/night temperature changes. Component 2 (in black) of the image indicates the annual temperature changes, and component 3 (in pink) almost shows the seasonal changes in this time series. Note that only a small portion of the annual (in black) and seasonal (in pink) components is shown in Fig. 3b, explaining why they look like trends, i.e., if one zooms out the entire annual and seasonal cycles will be visible.

For better visualization, the variances for each components are normalized and the results are illustrated in Fig. 4. This figure shows the three main components are in the steep section of the plot, showing the significant signal components have a large total variance. Eigenvalues 1 to 3, located in the steep part of the graph, represent the signal part of the spectrum (useful data) and constitute 98 % (first mode 50 %, second mode 47 %, third mode 1 %) of the variance of the data. When the window size increases to the values of 180 (about three months), 360 (about six months) and 720 (about one year), there is no significant change in the number of significant components, but the variance of the third state increases and reaches 9 %, 25 %, 26 %, respectively (Fig. 4).

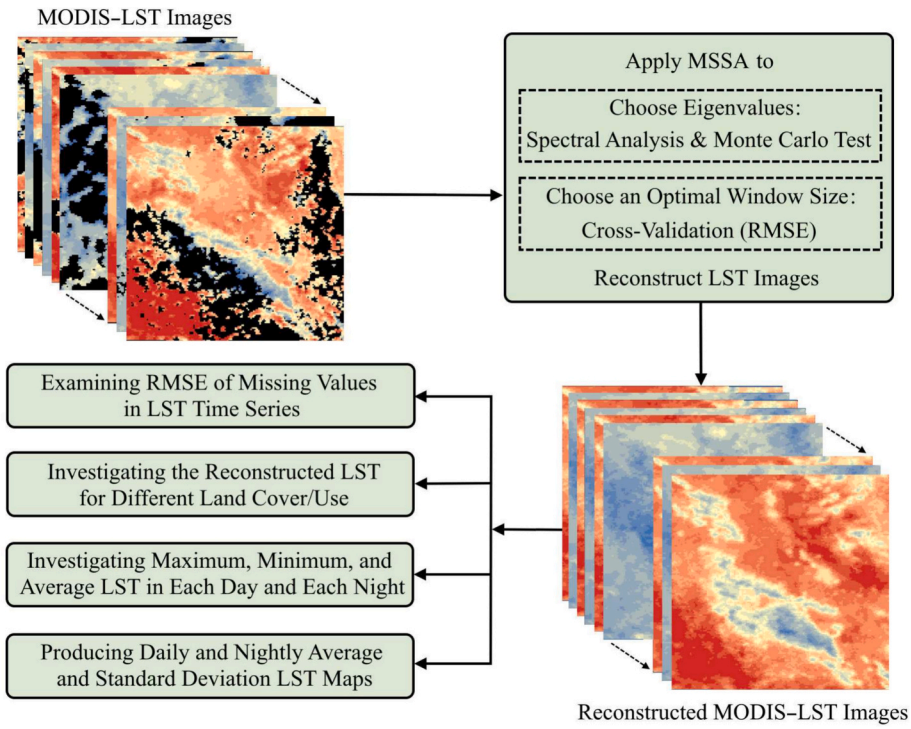

Fig. 2. Flowchart of this study: the steps of reconstruction of MODIS–LST time series using multi–channel singular spectrum analysis (MSSA) and their validations. The gaps in images are shown in black. The LST and RMSE are short for land surface temperature and root mean square error, respectively.

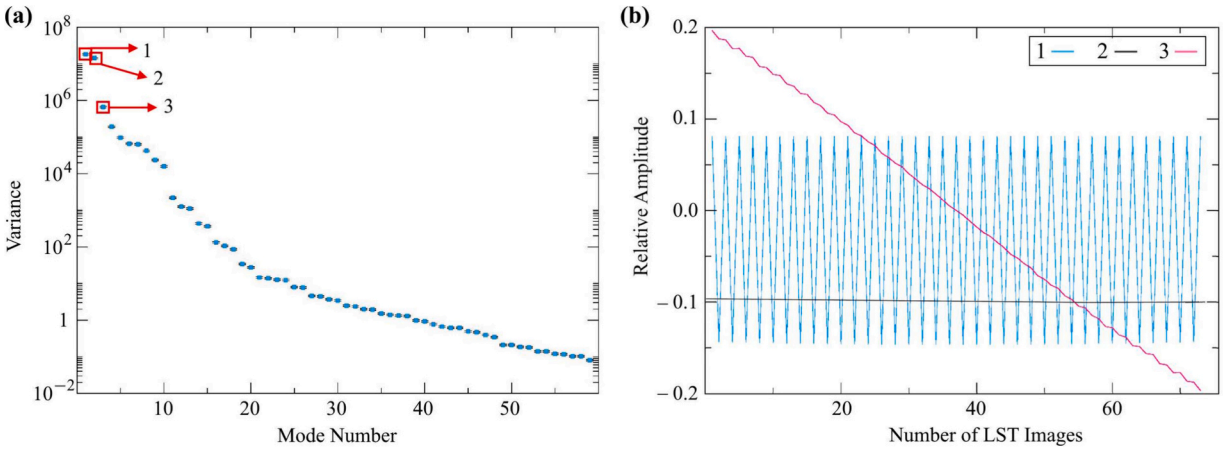

Fig. 3. (a) The spectrum of eigenvalues of data with a window size 60, where the red arrows show the most significant components, and (b) Empirical–time orthogonal functions of the three significant components of MSSA with a window size 60. (For interpretation of the references to color in this figure legend, the reader is referred to the web version of this article.)

Pairs of SSA eigenvalues that are close to each other and also have a one-quarter (90°) phase difference can effectively represent a periodic oscillation in a time series. This is because a particular mode pair of a data adaptive method such as SSA can capture periodicity in fluctuating data. When a window size 720 is selected, components 2 and 3 are almost pairwise next to each other. To verify that these components are significantly related to the signal, the Monte Carlo test is conducted. The Monte Carlo test uses a first-order autoregressive process to generate alternative time series according to parameters determined from the series. Then, for each realization, SSA is employed to compute the eigenvalues. Next, error estimation is carried out at the 95 % confidence level to determine whether the eigenvalues are statistically significant. The eigenvalues on top of the error bar are statistically significant and show the important part of the spectrum (i.e., signal). The results of data analyses and the null hypothesis of EOFs are illustrated in Fig. 5. The panels demonstrate eigenvalue power and the replaced data values vs the frequency of EOFs. Given that SSA-induced EOFs for an inherently periodic time series are not fully sinusoidal, deriving a single frequency for each EOF is not an easy task. In other words, the SSA-induced EOFs for a periodic time series are not perfectly sinusoidal unless they consist of perfectly periodic components, e.g., time series of compound periods. Panel (a) in Fig. 5 shows the results of the Monte Carlo test with the original data and panel (b) with the null hypothesis EOFs test.

From Fig. 5, components 1, 2, and 3 are the most significant with a specific percentile of 97.5 %. In this figure, the components are sorted based on their associated variances. In other words, the frequencies of components 1, 2, and 3 are 0.494, 0.001, and 0.006 (cycles/day), belonged to daily, annual, and three-month periods, respectively. The

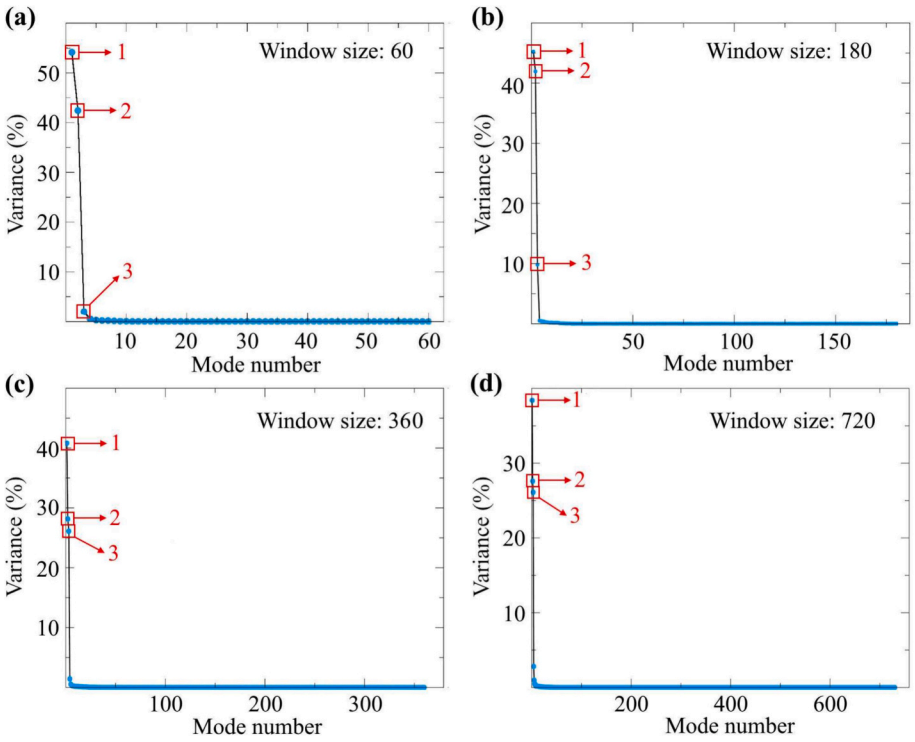

Fig. 4. The plot of normalized eigenvalues (variance changes for each component) for window size (a) 60, (b), 180, (c) 360, and (d) 720. The red arrows show the most significant components. (For interpretation of the references to color in this figure legend, the reader is referred to the web version of this article.)

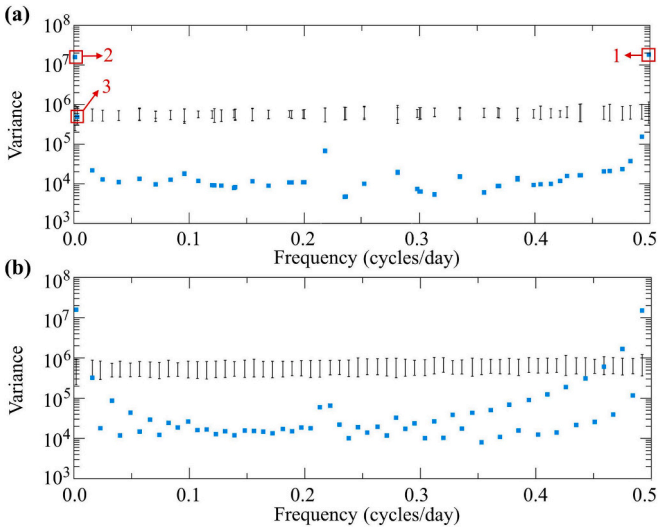

Fig. 5. The SSA Monte Carlo test based on (a) original data and (b) null hypothesis tests. The red arrows show the most significant frequencies. Note that the same y-axis is used to read the length of each error bar. (For interpretation of the references to color in this figure legend, the reader is referred to the web version of this article.)

EOFs of the null hypothesis test in Fig. 3b confirm the significance of the components. The advantage of the null hypothesis test is that it selects a noise component with low probability as a significant signal component. This feature helps to identify the main and significant signals and its results are more reliable.

3.2. Examining RMSE of missing values in LST time series

In addition to the results obtained from the previous tests, MSSA is applied to the seven-year-long time series of MODIS–LST with the sequence of day and night with the window sizes 60, 180, 360, and 720. Images are divided into several blocks before reconstruction. The MSSA is applied to each block individually. After running the algorithm, the blocks are connected to each other and the images are converted to the original dimensions. First, the comparison of the accuracy of land surface temperature reconstruction is carried out using the 4 mentioned windows in the LST images of the time series of 2014 (720 images) in order to compare the accuracy of the reconstruction in these windows. The RMSE image obtained by comparing the reconstructed LST using MSSA and different window sizes with the original MODIS–LST is prepared.

To examine the gap-filling performance of MSSA, in one-year time series of MODIS–LST images, twenty images without gaps related to day and night are selected from the images, and their values are removed from the time series, creating artificial gaps. The cloud data (data with zero value) are removed and not considered in RMSE calculation. Then gap–filling is performed by different window sizes in MSSA, and finally the reconstructed and initial values are used to compute the RMSE image by Eq. (8), see Fig. 6. The results show that by using the window size 60, about 92 % of the study region is reconstructed with an RMSE of less than 3 °C. From Fig. 6 one can observe that increasing the window size results in an increase in RMSE. For example, about 7 %, 12 %, 33 %, and 48 % of the region has RMSE greater than 3 °C for window sizes 60, 180, 360, and 720, respectively. Therefore, window size 60 is more accurate in reconstructing LST images. In addition to examining the entire image, the reconstructed values of the time series of LST with the sequence of day and night in different window sizes for the selected pixel (the star in Fig. 1) are compared with the initial values using MSSA (Fig. 7), showing a very good reconstruction result using window size 60 with RMSE of 1.4 °C.

Next, given that the percentage map of missing data in the MODIS–LST images and the RMSE image resulting from the reconstruction of the time series using MSSA is prepared in a categorized manner, the area of the categories of the gap percentage in each of the RMSE error

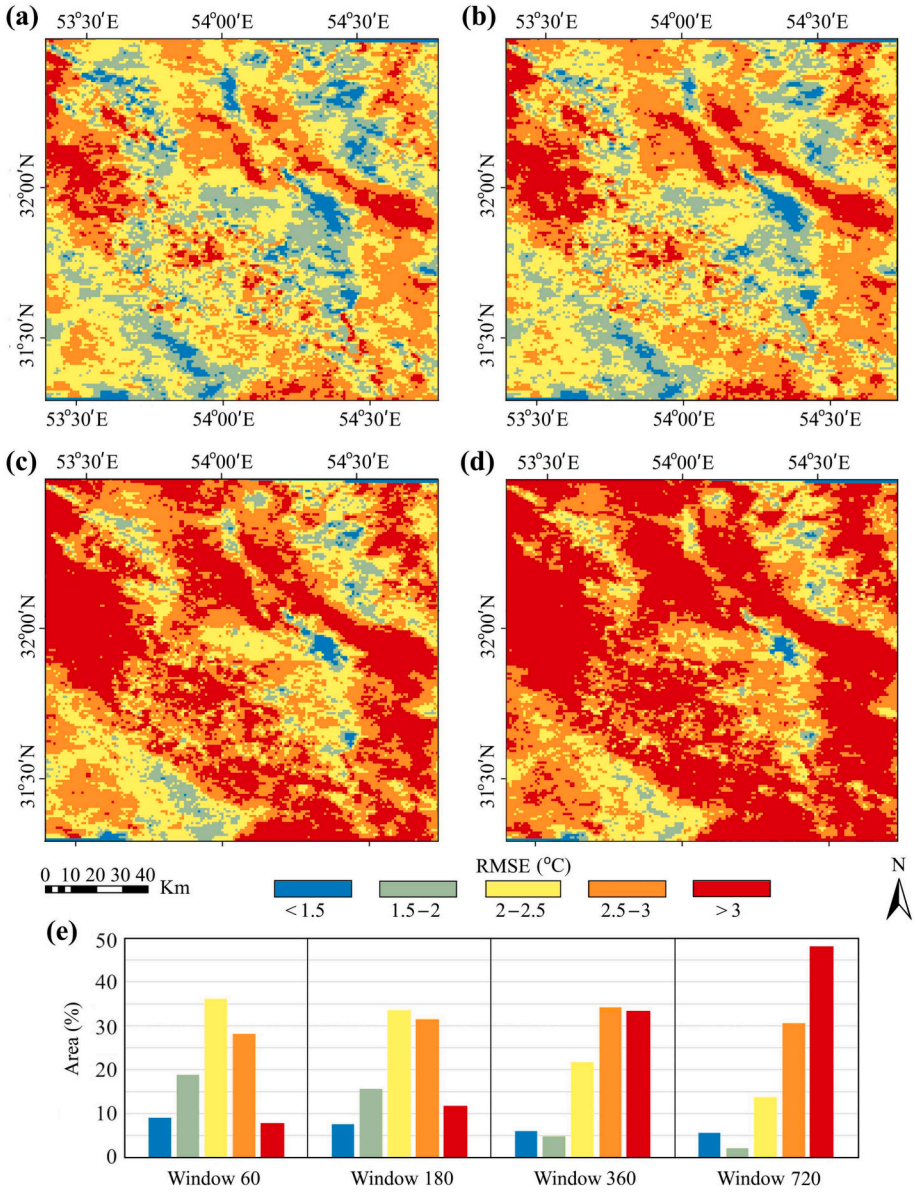

Fig. 6. The RMSE image for reconstructing the MODIS–LST images (°C) based on MSSA using window size: (a) 60, (b) 180, (c) 360, (d) 720, and (e) comparison of their percentage areas. The RMSE images are calculated based on true and reconstructed values. First, gaps are artificially created by removing 20 images, and then MSSA is applied to estimate the RMSE images.

categories is verified (Fig. 8). In every category with RMSE greater than 3 °C, there exists more than 24 % of missing data. The seven-year-long MODIS–LST time series are processed by MSSA with window size 60 (optimal) to fill in the missing values. An example of the day and night LST image before and after reconstruction is illustrated in Fig. 9, showing the areas covered by cloud and missing data have been completely reconstructed. Since LST during daytime is significantly different than LST during nighttime due to the desert nature of the study region, the same colormaps are used in Fig. 9 but with different value ranges for day and night to aid visualization.

3.3. Comparison between gap–filling performances of MSSA and HANTS

The HANTS is also applied to the same set of images used to obtain RMSE images in Fig. 7. As demonstrated by Arabi Aliabad et al. (2024), 19 frequencies are used in HANTS to reconstruct LST images and estimate the RMSE image, displayed in Fig. 10. The comparison results show that in gap–filling LST using HANTS, the use of LST images as a sequence of day and night cannot provide acceptable results and day and night images should be reconstructed separately. The HANTS reconstruction is based on the annual temperature cycle model (Arabi Aliabad et al., 2024). In LST image reconstruction using HANTS, only 4 % of the study region has been reconstructed with an RMSE less than 3 °C, while in MSSA with a window size 60, about 92 % of the area has been reconstructed with an RMSE less than 3 °C, see Fig. 10.

3.4. Investigating the reconstructed LST for different land cover/use classes

The reconstructed one-year time series of MODIS–LST are classified according to each land cover/use class, and the changes of daytime and nighttime LST for the classes are illustrated in Fig. 11. In bare lands, the nighttime LST decreases by almost 37 °C as compared to the daytime, while in rangelands and sand dune this decrease is 34.8 °C and 32.5 °C, respectively. Mountainous areas and residential lands have a lower temperature drop between day and night in the one-year time series, and

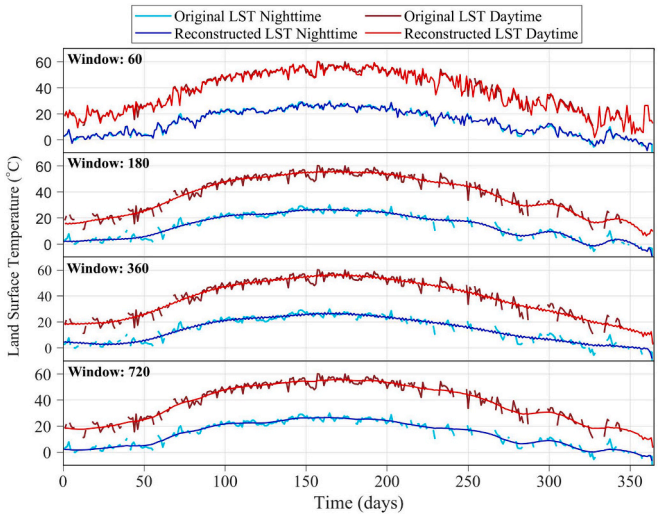

Fig. 7. Comparison of reconstructed LST (°C) for window sizes: (a) 60 (RMSE: 1.4 °C), (b) 180 (RMSE: 2.6 °C), (c) 360 (RMSE: 2.8 °C), and d) 720 (RMSE: 2.9 °C) at the selected pixel as an example. RMSE is short for root mean square error.

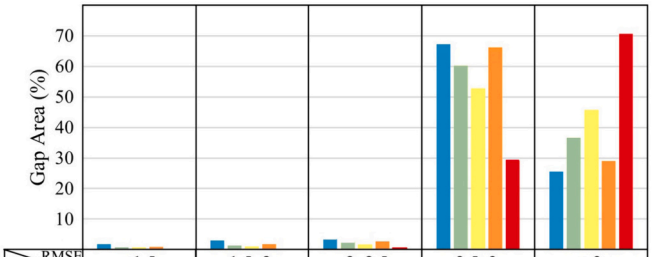

RMSE / M(%)	<1.5	1.5–2	2–2.5	2.5–3	>3
< 18	1.42	2.51	3.36	67.19	25.52
18–20	0.51	0.83	1.90	60.12	36.64
20–22	0.25	0.46	1.01	52.66	45.62
22–24	0.66	1.31	2.84	66.21	28.98
> 24	0.00	0.00	0.12	29.30	70.58

Fig. 8. Examining RMSE (°C) in each category of missing data, shown in different colors and labeled as M(%), in the seven-year-long time series of LST.

their LST at night decrease compared to the day by about 22 °C. *bare* lands, sand dune and rangelands show the highest daily LST during the one-year time series. LST in the agricultural areas during the summer does not generally follow the same pattern as other land covers, and they require more irrigation to prevent stress in this season. Unlike daytime, the analysis of nighttime LST images show that the highest LST at night in the whole year is related to residential land cover. In other words, compared to nighttime LST in other land covers, residential areas have higher LST during the night.

3.5. Estimating maximum, minimum, and average LST images in each day and night

The maximum, minimum, and average values of MODIS–LST in each day and night are calculated in the seven-year-long time series (2014–2020). Fig. 12 shows that the sinusoidal pattern in all the minimum, maximum, and average values of LST in day and night are well defined. The maximum, minimum, and average values of each LST image are calculated from the LST values between the 2nd and 98th percentiles of the LST image to reduce the effect of potential outliers. The average daytime and average nighttime LST images for spring, summer, fall, and winter and for period 2014–2020 are calculated and displayed in Fig. 13. Examining the average values of the daily LST images in the seven-year period shows that in the summer season, the average daily LST images is approximately 56 °C, while at night, it is about 24 °C. In other words, the average LST during the day and night of the study region differs by about 32 °C. The maximum MODIS–LST in the daily imagery in the summer season and the peak of heat is around 60 °C to 65 °C and in the coldest days of the year is around 22 °C. The maximum LST in the night time series images is between 28 °C and 30 °C during the peak of summer heat and between 9 °C and 11 °C in the coldest days of the year. Usually, there is no complete time series of minimum LST due to being located in mountainous areas and usually on top of mountains, but in this part, considering that LST has been reconstructed MSSA, it is possible to verify them. The daily minimum LST in the hot season is between 39 °C and 41 °C and at night is between 9 °C and 11 °C. In other words, in summer, there is about a 30 °C difference between day and night minimum LST.

3.6. Producing daily and nightly average and standard deviation LST maps

Using the reconstructed images of MODIS–LST in the seven-year-long time series, the average and standard deviation of the day and night LST images are estimated separately and illustrated in Fig. 14, showing that in 26 % of the study region, the LST range from 35 °C to 37 °C and 12 % of the study region had a temperature higher than 39 °C, and 7 % of the area had LST less than 25 °C. In general, in more than half of the region, the average LST in daily images is higher than 35 °C. The average nightly MODIS–LST map shows that about 58 % of the study region had a temperature more than 10 °C. At night, the average LST has decreased so much that only in 3 % of the region the LST is more than 14 °C, while during the day, 93 % of the region had an average temperature of above 25 °C. Considering that the study region is a desert, the big difference between day and night LST, as shown in the standard deviation maps, can be expected.

4. Discussion

4.1. The choice of window size in MSSA

Optimal selection of the window size is not an easy task in MSSA. As mentioned earlier, a large window size can capture longer period oscillations (low frequency components) in a data set, but a small window size, in contrast, increases the statistical significance because low and high frequency components will not compete for limited available variance. Note that the window sizes 60, 180, 360 and 720 are examined in detail in the present research because these window sizes respectively correspond to the monthly, seasonal, semi-annual and annual LST cycles that are usually the most dominant cycles in LST time series (Ahmed et al., 2023; Ghaderpour et al., 2023). Other window sizes, such as 30, 90, 120 and 150 were also examined, and the RMSE results of the entire study region and the selected pixel were also estimated. Table 2 summarizes the RMSE results of eight different window sizes examined in this research, where the results of window sizes 60, 180, 360 and 720 were demonstrated in more detail in the present study. Window sizes less than 60 did not provide acceptable results, and window size 60 had the lowest RMSE with a faster computational speed compared to larger window sizes.

To reconstruct the MODIS–LST images with day and night sequence using MSSA over seven years, the processing is carried out separately for each year. To process the images with window size 180, the images are divided into two blocks each year. To process images with window sizes 360 and 720, the images are divided into 4 and 8 blocks, respectively. Note that this division is carried out only due to the computer RAM limitation. Since the nature of LST time series is periodic, the main shape specified by SSA is also periodic functions. As observed in Fig. 4, by enlarging the window size, the number of significant components does

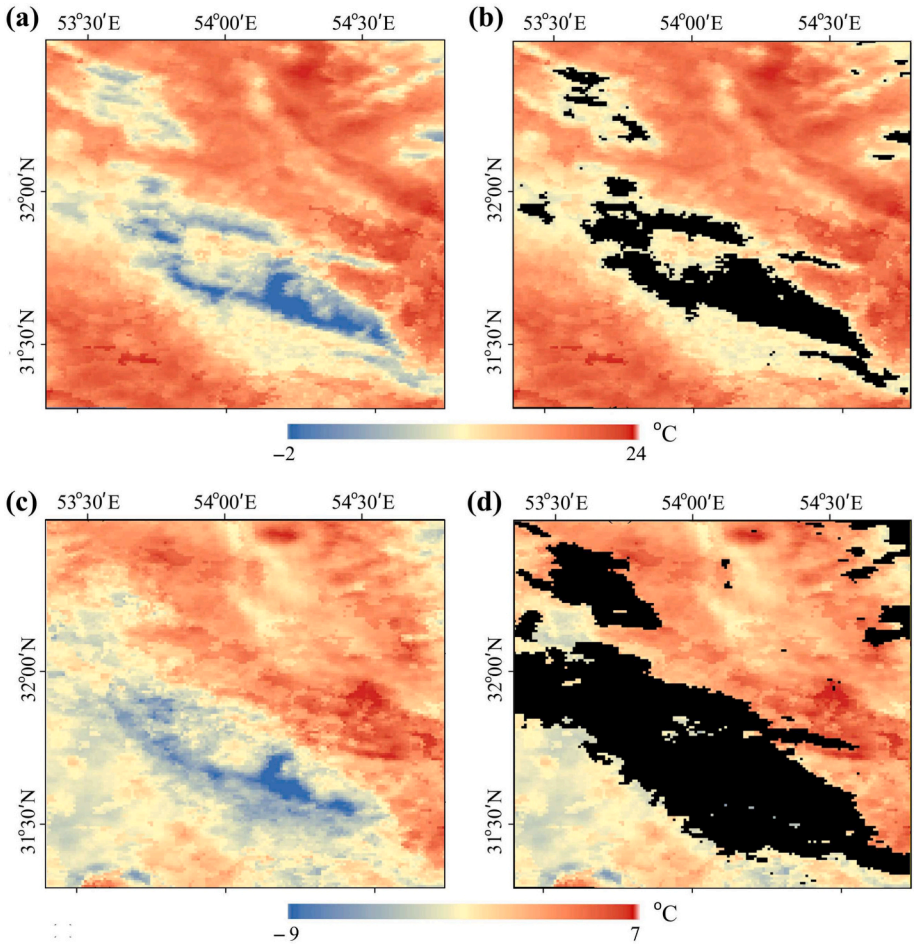

Fig. 9. (a) Image of the daily LST reconstructed using MSSA in a seven-year period, (b) Original daily LST with data gaps, (c) Image of the nightly LST reconstructed using MSSA in a seven-year period, (d) Original nightly LST with data gaps. The top colorbar ranging from −2 °C to 24 °C is used for panels (a) and (b), and the bottom colorbar ranging from −9 °C to 7 °C is used for panels (c) and (d).

not change, but all three components of the total variance of the data change. Correlation coefficient is also estimated at 99 % for window size 60 using MSSA and 97 % in other window sizes.

4.2. Sensitivity of MSSA to missing data

The MSSA is a powerful technique for decomposing time series data into trend, seasonal, and noise components. While it is robust to some degrees of missing data, the impact of continuous, spatially large missing areas can vary depending on the following factors.

(i) Spatial extent of missing area: If the missing area is relatively small and localized, MSSA may be able to interpolate values from neighboring pixels or nearby time steps. However, large, continuous missing areas can significantly disrupt the spatial coherence of the data and make accurate reconstruction more challenging.
(ii) Temporal duration of missing data: Short-term missing data gaps might be less problematic because MSSA can use information from surrounding time steps to fill in the missing values. Long-term missing data can be more detrimental as it can affect the estimation of trend and seasonal components.
(iii) Data characteristics: The characteristics of MODIS data, such as spatial resolution, temporal frequency, and noise levels can influence the impact of missing data. For example, higher spatial resolution data may be more sensitive to missing data, while lower noise levels can improve reconstruction accuracy.
(iv) MSSA parameters: The choice of MSSA parameters, such as the number of singular values and the window size can also affect the algorithm's sensitivity to missing data. In general, the longer the time series is, the better the results will be, and this is why the seven-year-long time series is used in this research. Also, the presence of a gap at the beginning and end of the time series period can cause more errors than the presence of a gap in the middle of the time series.

4.3. Comparison of MSSA with HANTS for LST image reconstruction

Arabi Aliabad et al. (2024) demonstrated the capability of HANTS in reconstructing time series images of daytime and nighttime MODIS–LST for the same study region. They showed that HANTS faced limitations in accurately reconstructing the day-night sequence, particularly due to temperature disparities between day and night. Consequently, separate LST image reconstructions for day and night using HANTS showed an improved accuracy for the study region. Arabi Aliabad et al. (2024) also found that with 15 and 19 frequencies and a minimum period of 2 images, HANTS is suitable for daily and nightly MODIS–LST reconstruction in the study region. In Fig. 10, the average RMSE of HANTS is about 5.3 °C, while the average RMSE of MSSA with window size 60 is about 2.6 °C, indicating the superiority of MSSA for reconstructing daytime and nighttime MODIS–LST images. In addition, RMSE between the original and reconstructed LST time series for the same selected pixel using HANTS and MSSA are 4.5 °C and 1.4 °C, respectively. The reconstruction performance of the MODIS–LST images also agree with

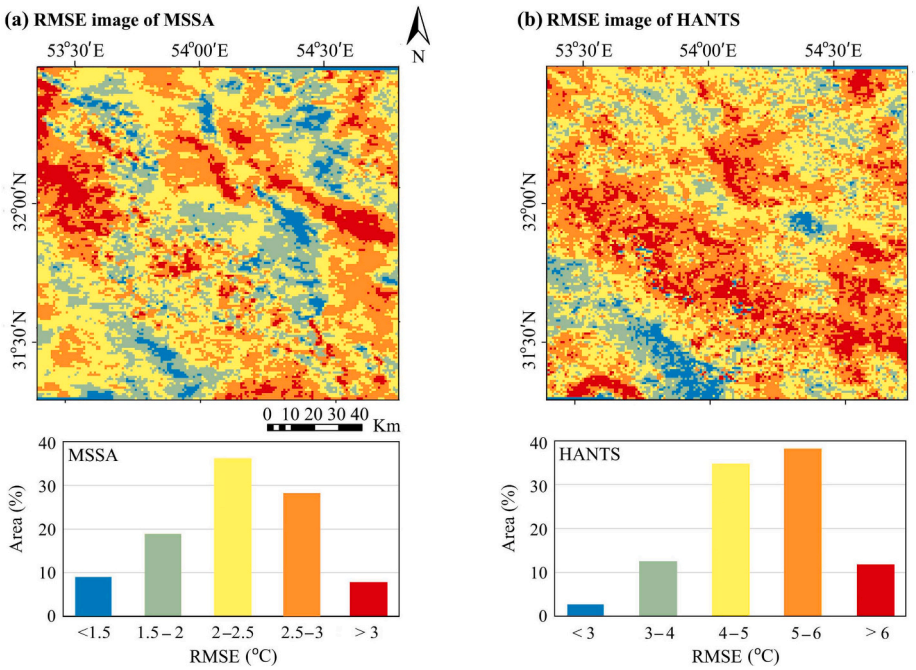

Fig. 10. Comparison between MSSA and HANTS using their optimal parameter values: (a) RMSE image using MSSA for window 60 (same as Fig. 6a to aid side-by-side comparison with HANTS), and (b) RMSE image using HANTS with 19 frequencies. To aid visualizing different RMSE classes in the maps, the same color schemes are used in panel (a) and (b) (both maps and bar charts) but with different value ranges, i.e., for each color, the RMSE range for HANTS is twice more than the one for MSSA.

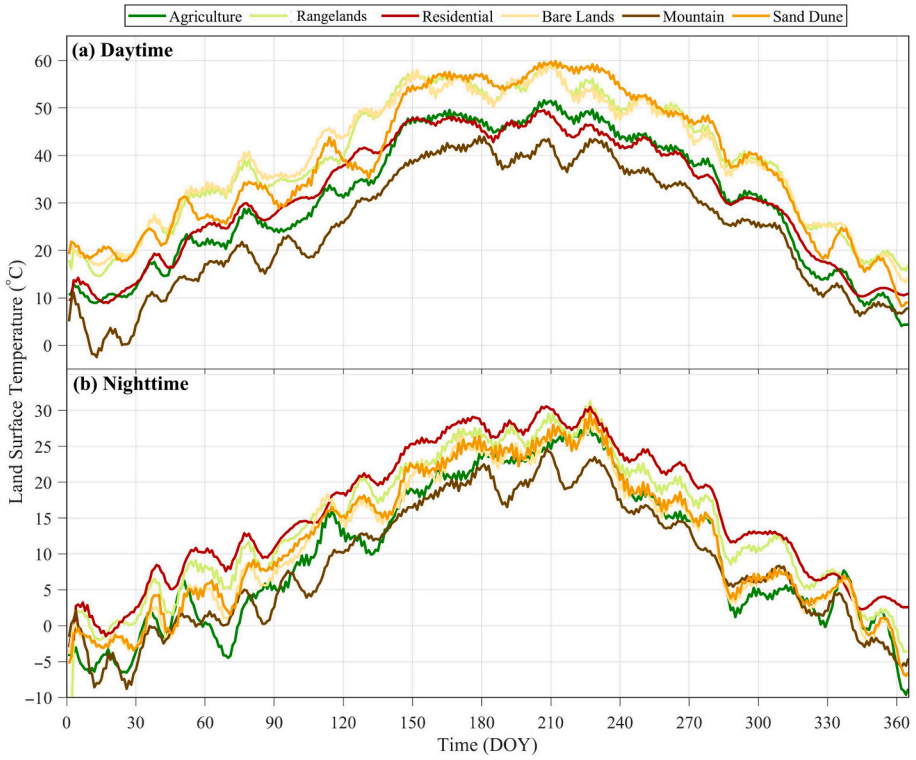

Fig. 11. Changes in MODIS–LST (°C) in different land covers: (a) daytime, and (b) nighttime.

Alfieri et al. (2013) and Ghafarian Malamiri et al. (2018) who stated that MSSA can use the spatiotemporal correlation for an effective gap–filling. The findings of the present research are in good agreement with those of Menenti et al. (2016) who investigated the application of MSSA and HANTS in reconstructing MODIS–LST. Their results showed that MSSA is capable of reconstructing LST with high accuracy. The reason for achieving this accuracy is that MSSA considers both spatial and temporal information of LST images while HANTS only considers the temporal information of LST images. In other words, HANTS reconstructs per-pixel time series independently while MSSA also uses the

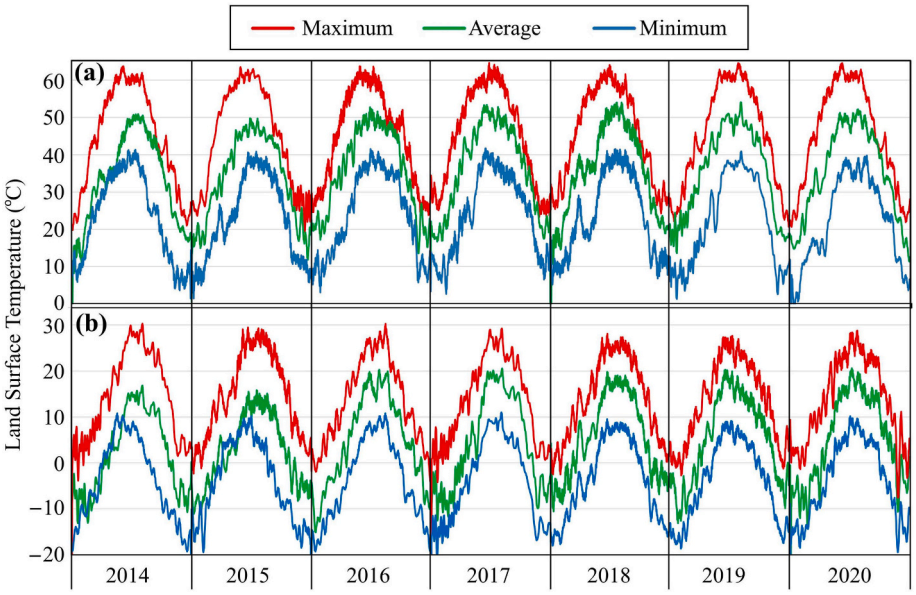

Fig. 12. Examining changes in average, maximum, and minimum LST (°C) in reconstructed images using MSSA: (a) daytime, and (b) nighttime.

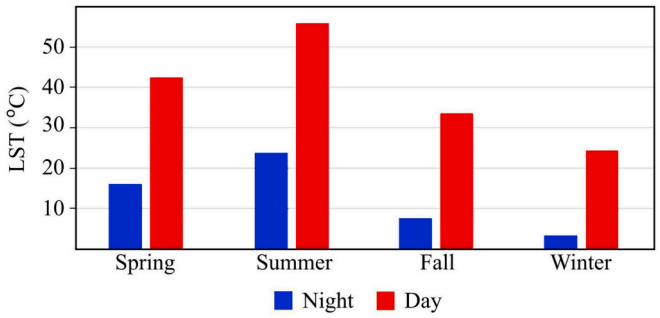

Fig. 13. The average daytime and average nighttime LST images for different seasons during 2014–2020.

information of neighboring clear–sky pixels for reconstructing LST which is more effective especially for constructing time series with long temporal gaps.

Compared with temporal gap–filling models, such as HANTS, MSSA is more complex and has a higher computational cost. Due to the high volume of processes in MSSA, it is sometimes necessary to divide the images into several smaller blocks and reconnect after processing. In image reconstruction using MSSA, the longer the time series is, the more accurate the reconstruction accuracy will be. The presence of missing data at the beginning and end of the time series generally reduces the accuracy of the reconstruction. The MSSA is a linear technique to analyze and predict the behavior of a time series. It is a non-parametric method compatible with the data, and this is one of the advantages of MSSA over classical spectral methods, such as Fourier series analysis. The HANTS is a temporal Fourier-based method that works well when the time series is clearly a mixture of periodic components. When the time series contains some periodic components, it needs many frequencies to reconstruct the time series. In Fourier series analysis, periodic components are applied, while in MSSA, elementary components are extracted from the data. This means that if the time series contains intrinsic components, the SSA decomposition will also be periodic. The data adaptive nature of MSSA makes it suitable for analyzing nonlinear dynamics, since there are no assumptions about the underlying physical processes that govern the observed time series. Therefore, it can be applied to any type of time series.

4.4. Validation of the LST results

Validating the LST results is a challenging task due to the lack of LST ground database as pointed out by Adeniran et al. (2024). The hourly air and surface temperature records (ground-based) in a summer day for the selected pixel (the star in Fig. 1d), are illustrated in Fig. 15. Due to climatic conditions (e.g., wind), the air temperature pattern does not match very well with the surface temperature pattern; however, there is a good agreement between the reconstructed MODIS–LST and ground-based surface temperature measurements, see the red circles and yellow squares in Fig. 15. In the current research, in addition to validation by creating artificial gaps, as explained in Section 3.2, the reconstructed MODIS–LST values are also further validated by the field survey done by the authors through a thermometer as illustrated and documented in Arabi Aliabad et al. (2023b, Fig. 5). Note that the air and surface temperature measurements acquired by ground-based instruments are very localized and may not be a good proxy for a larger area, e.g., at the scale of one square kilometer that is the resolution of MODIS–LST, bringing another challenge for validation.

4.5. LST variation for land cover/use classes

The results of the daily LST in different land covers show that the lowest temperature in the whole year is related to the mountain land cover, see Fig. 11. After the mountains, the lowest LST is related to residential areas. Bare lands, sand dune, and rangelands had the highest daily LST during the one-year time series. The LST in the agricultural cover in the peak of heat and summer season did not have the same pattern as other land covers, demanding more irrigation in this season to avoid tension. The pattern of LST changes in different land covers in the day and night time series is different. Contrary to the day, the analysis of the time series of images of LST shows that the highest LST at night in the whole year is related to residential land cover, so that other land covers lost their temperature at night, but the temperature has slightly decreased in residential areas. It is found that the difference in temperature between day and night in different land covers is not the same throughout the year. The biggest difference between LST during day and night is due to the hot days of the year. The temperature of rangelands, sand dunes, and bare land covers shows the highest change in day and night LST compared to other covers. The change of night and day LST in different land covers is due to the reaction of a material to the changes in

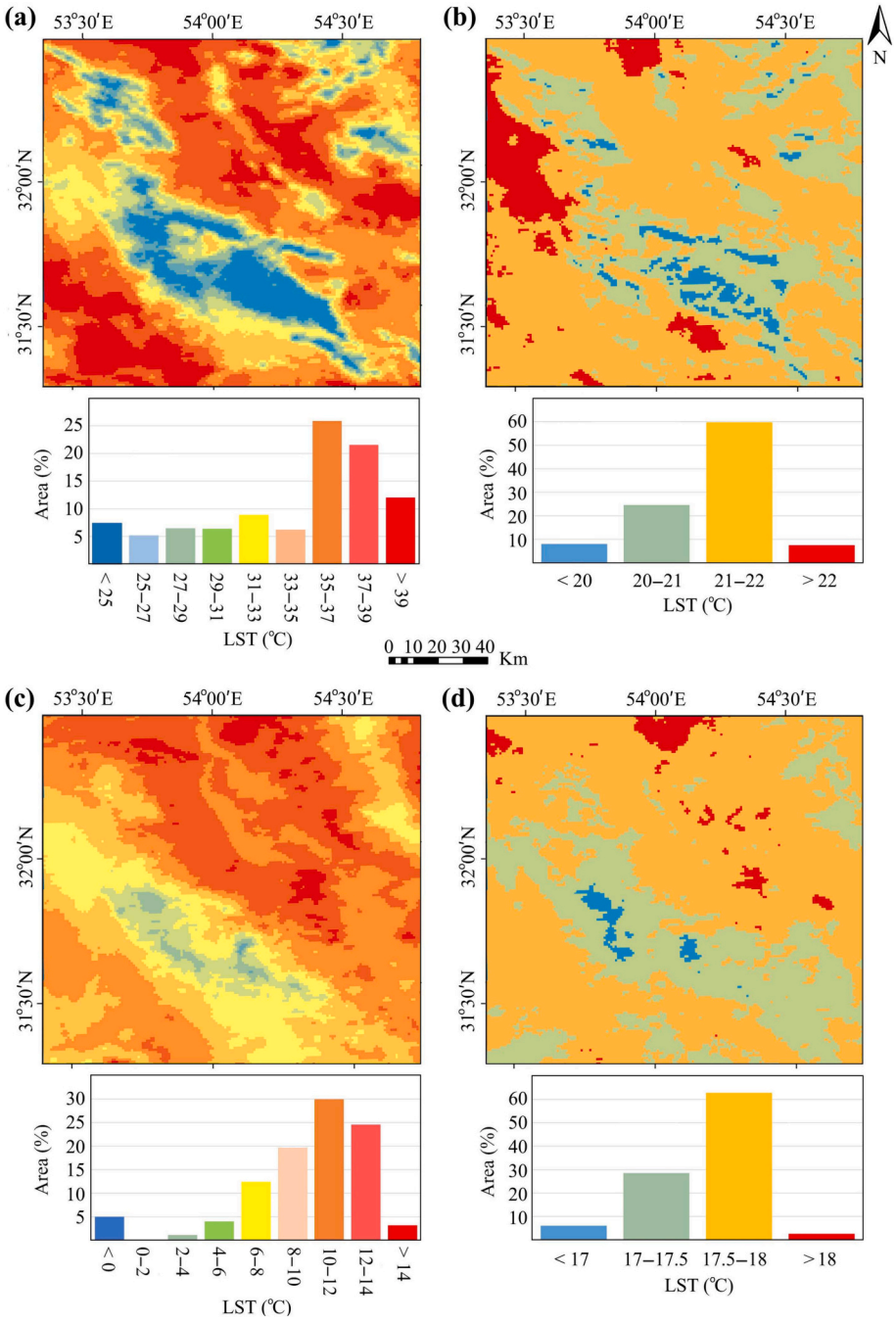

Fig. 14. (a)–(b) The average and standard deviation images of daily MODIS–LST, and (c)–(d) the average and standard deviation images of the nightly MODIS–LST (°C), respectively. The bar charts under each geospatial map shows the percentage area of each class with the same color scheme as in the map.

Table 2
The RMSE (°C) results of different window sizes for MSSA. The bold values are the best values.

Window size	30	**60**	90	120	150	180	360	720
RMSE of the study region	5.76	**2.60**	3.16	3.71	4.63	4.83	5.20	5.39
RMSE of the selected pixel	2.96	**1.40**	2.56	2.00	2.30	2.60	2.80	2.91

temperature or their thermal inertia property. Estimating and utilizing land surface emissivity may further improve LST estimation (Yan et al., 2024).

The results of LST changes in different land covers (see Fig. 11) showed that, the daytime LST in urban land is lower than the one in rangelands, bare lands and sand dune, which agree with the results presented by Tahooni et al. (2023) as their results indicated that reflective surfaces can increase albedo and decrease the surface temperature more efficiently than vegetation. The presented results indicated that urban growth and the impervious surfaces expansion could produce urban cold islands instead of heat islands if the rooftops have reflective surfaces.

4.6. LST variation during 2014–2020

The results of comparing the average LST in a seven-year time series

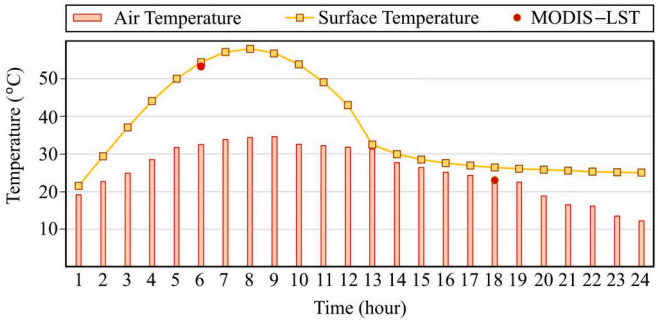

Fig. 15. Comparison of the reconstructed MODIS–LST with air temperature and ground-based surface temperature in a summer day for a pixel around the weather station. The hours on the x-axis start from 5:00 AM, the first hour after the sunrise.

(Fig. 12) demonstrate that in 2014, the average temperature of daily images is 32.58 °C and in 2015 it is 33.4 °C, while in 2019 and 2020 it is estimated to be 35.3 °C and 35.1 °C, respectively. In addition, the examination of the average LST in each daily image in the seven-year-long time series also shows that the maximum average value of the LST images in 2014 is 50.8 °C and in 2019 and 2020 are 54.2 °C and 53.7 °C, respectively, in agreement with gradual Earth surface temperature increase and global warming.

In winter, the minimum daily LST is estimated to be 0 °C to 3 °C for the study region. In the time series of night images, the minimum LST in this season is estimated to be −15°C. Considering that in the study area, all meteorological stations are located in the plains, and it is not possible to take land samples in the mountains using a thermometer. Therefore, it is not possible to estimate the minimum temperature to validate LST at night in the cold season – one of the limitations of this study. Among the four window sizes (60, 180, 360, 720) examined in the present study, it is found that window size 60 is the most optimal size that can reconstruct the LST time series very well. Smaller window sizes than 60, such as 20 and 30 are also examined but could not reconstruct the large data gaps well because they are too small to capture adequate data for computation.

4.7. *Practical implications of the reconstructed MODIS–LST images*

A complete time series of LST is required in many environmental science applications, such as deriving climatic indices and modelings. Using MSSA, it is possible to reconstruct LST images with acceptable accuracy and estimate the values that are missed due to the presence of clouds, dust and sensor problems. In climate studies, gaps in time series can significantly bias the trend estimation (Ahmed et al., 2023). To estimate drought stress in plants, surface energy algorithms, such as surface energy balance algorithm for land and surface energy balance system can be utilized, where LST image is a main component (Zamani Losgedaragh and Rahimzadegan, 2018). Therefore, to check the drought stress status of plants in the time series, it is necessary to reconstruct the LST images. Today, in urban areas, especially in desert areas, such as the studied region, important topics are global warming and thermal islands. In studies of heat islands, comparing the temperature in two days of the year with another year cannot well express the temperature change, so a time series should be compared. The first requirement for such investigations is the existence of a complete time series of LST, so it is necessary to reconstruct the temperature images first before proceeding to the next steps.

The complete series of LST, obtained from the reconstruction and gap–filling of the images in the present study can be used as input data in various applications, such as soil moisture estimation (Przeździecki et al., 2023), temperature trends (Ghaderpour et al., 2024; Shawky et al., 2023), retrieving evapotranspiration (Pan et al., 2024), plant stress monitoring (Guo et al., 2023), and urban heat islands (Almeida et al., 2021; Wang et al., 2021). Rapid urbanization in recent decades, accompanied by the rapid conversion of natural landscapes to impervious surfaces, has resulted in many ecological and environmental problems. The UHI and air pollution, typical problems in urban environments, have increased with the development of rapid urbanization (Xiang et al., 2022). Importantly, more than 50 % of the Earth population and 80 % of its economic activity is located in built-up areas, where urban heat is even more pronounced (Guo et al., 2023). Therefore, the mitigation of UHIs as well as their consequent effects on urban residents has become an important topic in the domain of urban climatology, landscape ecology, and planning (Samson Udama Eneche et al., 2024).

5. Conclusions

The time series of LST images obtained from satellites are used in various fields and used as the main input data in many models. However, these images have missing data due to the presence of clouds, dust, sensor defects, and others. Obtaining the complete time series of LST and reconstructing the missing data in these images is very important and challenging. In this research, MSSA is utilized to fill the missing data in MODIS–LST imagery. The results show that MSSA had a good accuracy in reconstructing MODIS–LST with the sequence of day and night when a window size 60 is chosen. The average RMSE of MSSA is estimated to be approximately 2.6 °C for the entire study region and 1.4 °C for the selected pixel, indicating a very good capability for reconstructing LST images and creating a complete time series of surface temperature without missing data and gaps. It is also shown that MSSA outperformed HANTS by about 2.7 °C (RMSE) for reconstructing MODIS–LST images. It is found that mountainous regions had the lowest daily LST, and the highest nightly LST is in residential areas. In addition, rangelands, sand dune, and bare lands had the highest day and night LST variation compared to other land covers. Considering that the presence of clouds and the creation of missing data can make time series images of LST unusable, studies concerned with reconstruction of LST and improving the existing methods to improve their accuracy are very useful. The results presented in this research indicate that MSSA is a powerful approach to the study of time-dependent phenomena. It combines elements of classical time series analysis, multivariate statistics, dynamical systems and signal processing. It is well suited for the analysis of time series with quasi-periodic behavior, where the amplitude or phase of oscillatory modes is modulated in time; both types of modulation are typical in the geosciences in general, and in space physics in particular. In future, other advanced machine learning and deep learning techniques can be utilized for LST image reconstruction and comparison with MSSA results.

CRediT authorship contribution statement

Fahime Arabi Aliabad: Writing – original draft, Visualization, Validation, Software, Methodology, Formal analysis, Data curation, Conceptualization. **Mohammad Zare:** Writing – review & editing, Supervision, Conceptualization. **Hamidreza Ghafarian Malamiri:** Writing – review & editing, Supervision, Conceptualization. **Amanehalsadat Pouriyeh:** Writing – review & editing, Data curation, Conceptualization. **Himan Shahabi:** Writing – review & editing, Supervision, Conceptualization. **Ebrahim Ghaderpour:** Writing – original draft, Visualization, Validation, Supervision, Funding acquisition, Conceptualization. **Paolo Mazzanti:** Writing – review & editing, Supervision, Funding acquisition, Conceptualization.

Declaration of competing interest

The authors declare that they have no known competing financial interests or personal relationships that could have appeared to influence the work reported in this paper.

Data availability

The code, input and output datasets, including the guideline on how to run the code can be found online at the following link: https://github.com/Fahimearabi/Reconstruction-of-LST-images-using-MSSA.

Acknowledgment

This work was supported by CERI Research Centre at Sapienza University of Rome. The authors thank the NASA scientists and personnel for providing MODIS–LST imagery used in this work and thank the reviewers for their constructive suggestions.

References

Adeniran, I.A., Nazeer, M., Wong, M.S., Zhu, R., Yang, J., Chan, P.W., 2024. Improved fusion model for generating hourly fine scale land surface temperature data under all-weather condition. Int. J. Appl. Earth Obs. Geoinf. 131, 103981.
Agam, N., Kustas, W.P., Anderson, M.C., Li, F., Colaizzi, P.D., 2008. Utility of thermal image sharpening for monitoring field-scale evapotranspiration over rainfed and irrigated agricultural regions. Geophys. Res. Lett. 35, L02402.
Ahmed, M.R., Ghaderpour, E., Gupta, A., Dewan, A., Hassan, Q.K., 2023. Opportunities and challenges of spaceborne sensors in delineating land surface temperature trends: a review. IEEE Sensors J. 23, 6460–6472.
Alfieri, S.M., De Lorenzi, F., Menenti, M., 2013. Mapping air temperature using time series analysis of LST: the SINTESI approach. Nonlin. Processes Geophys. 20, 513–527.
Aliabad, F.A., Shojaei, S., Mortaz, M., Ferreira, C.S.S., Kalantari, Z., 2022. Use of Landsat 8 and UAV images to assess changes in temperature and evapotranspiration by economic trees following foliar spraying with light-reflecting compounds. Remote Sens. 14, 6153.
Allen, M.R., 1992. Interactions between the Atmosphere and Oceans on Time Scales of Weeks to Years. Ph.D. thesis. University of Oxford.
Almeida, C., Teodoro, A., Gonçalves, A., 2021. Study of the urban heat island (UHI) using remote sensing data/techniques: a systematic review. Environments 8, 105.
Almeida, C., Furst, L., Gonçalves, A., Teodoro, A., 2022. Remote sensing image-based analysis of the urban heat island effect in Braganca, Portugal. Environments 9, 98.
Arabi Aliabad, F., Ghafarian Malamiri, H., Sarsangi, A., Sekertekin, A., Ghaderpour, E., 2023a. Identifying and monitoring gardens in urban areas using aerial and satellite imagery. Remote Sens. 15, 4053.
Arabi Aliabad, F., Zare, M., Ghafarian Malamiri, H., Ghaderpour, E., 2023b. Improving the accuracy of landsat 8 land surface temperature in arid regions by MODIS water vapor imagery. Atmosphere 14, 1589.
Arabi Aliabad, F., Shojaei, S., Zare, M., Ghafarian Malamiri, H., 2024. Investigating the Capability of the Harmonic Analysis of Time Series (HANTS) Algorithm in Reconstructing Time Series Images of Daytime and Nighttime Land Surface Temperature from the MODIS Sensor. Spat. Inf. Res.
Broomhead, D.S., King, G.P., 1986. On the Qualitative Analysis of Experimental Dynamical Systems. Adam Hilger Bristol.
Buo, I., Sagris, V., Jaagus, J., 2021. Gap-filling satellite land surface temperature over heatwave periods with machine learning. IEEE Geosci. Remote Sens. Lett. 19, 1–5.
Chander, G., Markham, B.L., Helder, D.L., 2009. Summary of current radiometric calibration coefficients for Landsat MSS, TM, ETM+, and EO-1 ALI sensors. Remote Sens. Environ. 113, 893–903.
Cho, D., Yoo, C., Im, J., Lee, Y., Lee, J., 2020. Improvement of spatial interpolation accuracy of daily maximum air temperature in urban areas using a stacking ensemble technique. GISci. Remote Sens. 57, 633–649.
Cho, D., Bae, D., Yoo, C., Im, J., Lee, Y., Lee, S., 2022. All-sky 1 km MODIS land surface temperature reconstruction considering cloud effects based on machine learning. Remote Sens. 14, 1815.
Dousset, B., Gourmelon, F., 2003. Satellite multi-sensor data analysis of urban surface temperatures and landcover. ISPRS J. Photogramm. Remote Sens. 58, 43–54.
Duan, S., Li, Z., Leng, P., 2017. A framework for the retrieval of all-weather land surface temperature at a high spatial resolution from polar-orbiting thermal infrared and passive microwave data. Remote Sens. Environ. 195, 107–117.
Duan, S.B., Li, Z.L., Li, H., Göttsche, F.M., Wu, H., Zhao, W., Leng, P., Zhang, X., Coll, C., 2019. Validation of collection 6 MODIS land surface temperature product using in situ measurements. Remote Sens. Environ. 225, 16–29.
Elsner, J.B., Tsonis, A.A., 1996. Singular Spectrum Analysis: A New Tool in Time Series Analysis. Springer Science & Business Media.
Fang, H., Liang, S., Kim, H.Y., Townshend, J.R., Schaaf, C.L., Strahler, A.H., Dickinson, R. E., 2007. Developing a Spatially Continuous 1 Km Surface Albedo Data Set over North America from Terra MODIS Products. J. Geophys. Res, Atmos, p. 112.
Fu, P., Weng, Q., 2018. Variability in annual temperature cycle in the urban areas of the United States as revealed by MODIS imagery. ISPRS J. Photogramm. Remote Sens. 146, 65–73.
Fu, H., Shao, Z., Fu, P., Huang, X., Cheng, T., Fan, Y., 2022. Combining ATC and 3D-CNN for reconstructing spatially and temporally continuous land surface temperature. Int. J. Appl. Earth Obs. 108, 102733.
Ghaderpour, E., Mazzanti, P., Scarascia Mugnozza, G., Bozzano, F., 2023. Coherency and phase delay analyses between land cover and climate across Italy via the least-squares wavelet software. Int. J. Appl. Earth Obs. Geoinf. 118, 103241.
Ghaderpour, E., Mazzanti, P., Bozzano, F., Scarascia Mugnozza, G., 2024. Trend analysis of MODIS land surface temperature and land cover in Central Italy. Land 13, 796.
Ghafarian Malamiri, H., 2015. Reconstruction of Gap-Free Time Series Satellite Observations of Land Surface Temperature to Model Spectral Soil Thermal Admittance. Ph.D. thesis. Delft University of Technology.
Ghafarian Malamiri, H.R., Rousta, I., Olafsson, H., Zare, H., Zhang, H., 2018. Gap-filling of MODIS time series land surface temperature (LST) products using singular spectrum analysis (SSA). Atmosphere 9, 334.
Ghafarian Malamiri, H.R., Zare, H., Rousta, I., Olafsson, H., Izquierdo Verdiguier, E., Zhang, H., Mushore, T.D., 2020. Comparison of harmonic analysis of time series (HANTS) and multi-singular spectrum analysis (M-SSA) in reconstruction of long-gap missing data in NDVI time series. Remote Sens. 12, 2747.
Ghafarian, H.R., Menenti, M., Jia, L., den Ouden, H., 2012. Reconstruction of cloud-free time series satellite observations of land surface temperature. EARSel eProc. 11, 123–131.
Ghil, M., Allen, M.R., Dettinger, M.D., Ide, K., Kondrashov, D., Mann, M.E., Robertson, A. W., Saunders, A., Tian, Y., Varadi, F., Yiou, P., 2002. Advanced spectral methods for climatic time series. Rev. Geophys. 40, 1003.
Golyandina, N., Zhigljavsky, A., 2013. Singular Spectrum Analysis for Time Series Springerbriefs in Statistics. Springer, Berlin, Heidelberg.
Golyandina, N., Nekrutkin, V., Zhigljavsky, A.A., 2001. Analysis of Time Series Structure: SSA and Related Techniques. CRC Press.
Guo, A., He, T., Yue, W., Xiao, W., Yang, J., Zhang, M., Li, M., 2023. Contribution of urban trees in reducing land surface temperature: evidence from china's major cities. Int. J. Appl. Earth Obs. Geoinf. 125, 103570.
Gupta, V., Ramani, N., 1980. Some aspects of regional-residual separation of gravity anomalies in a precambrian terrain. Geophysics 45, 1412–1426.
Hall, D.K., Comiso, J.C., DiGirolamo, N.E., Shuman, C.A., Key, J.R., Koenig, L.S., 2012. A satellite-derived climate-quality data record of the clear-sky surface temperature of the Greenland ice sheet. J. Clim. 25, 4785–4798.
Hengl, T., Heuvelink, G.B., Perčec Tadić, M., Pebesma, E.J., 2012. Spatio-temporal prediction of daily temperatures using time-series of MODIS LST images. Theor. Appl. Climatol. 107, 265–277.
Hu, D., Guo, F., Meng, Q., Schlink, U., Wang, S., Hertel, D., Gao, J., 2024. A novel dual-layer composite framework for downscaling urban land surface temperature coupled with spatial autocorrelation and spatial heterogeneity. Int. J. Appl. Earth Obs. Geoinf. 130, 103900.
Jia, A., Ma, H., Liang, S., Wang, D., 2021. Cloudy-sky land surface temperature from VIIRS and MODIS satellite data using a surface energy balance-based method. Remote Sens. Environ. 263, 11256.
Jiang, G.M., Li, Z.L., 2008. Split-window algorithm for land surface temperature estimation from MSG1-SEVIRI data. Int. J. Remote Sens. 29, 6067–6074.
Jolliffe, I.T., 1990. Principal component analysis: a beginner's guide—I. Introduction and application. Weather 45, 375–382.
Julien, Y., Sobrino, J.A., Verhoef, W., 2006. Changes in land surface temperatures and NDVI values over europe between 1982 and 1999. Remote Sens. Environ. 103, 43–55.
Kondrashov, D., Shprits, Y., Ghil, M., 2010. Gap filling of solar wind data by singular spectrum analysis. Geophys. Res. Lett. 37.
Kustas, W., Anderson, M., 2009. Advances in thermal infrared remote sensing for land surface modeling. Agric. For. Meteorol. 149, 2071–2081.
Li, X., Zhou, Y., Asrar, G.R., Zhu, Z., 2018. Creating a seamless 1 km resolution daily land surface temperature dataset for urban and surrounding areas in the conterminous United States. Remote Sens. Environ. 51, 84–97.
Li, H., Li, R., Yang, Y., Cao, B., Bian, Z., Hu, T., Du, Y., Sun, L., Liu, Q., 2021. Temperature-based and radiance-based validation of the collection 6 MYD11 and MYD21 land surface temperature products over barren surfaces in northwestern China. IEEE Trans. Geosci. Remote Sens. 59, 1794–1807.
Li, Z.L., Wu, H., Duan, S.B., Zhao, W., Ren, H., Liu, X., Leng, P., Tang, R., Ye, X., Zhu, J., Sun, Y., Si, M., Liu, M., Li, J., Zhang, X., Shang, G., Tang, B.H., Yan, G., Zhou, C., 2023. Satellite remote sensing of global land surface temperature: definition, methods, products, and applications. Rev. Geophys. 61, e2022RG000777.
Liu, Z., Zhan, W., Lai, J., Hong, F., Quan, J., Bechtel, B., Huang, F., Zou, Z., 2019. Balancing prediction accuracy and generalization ability: a hybrid framework for modelling the annual dynamics of satellite-derived land surface temperatures. ISPRS J. Photogramm. Remote Sens. 151, 189–206.
McMillin, L.M., 1975. Estimation of sea surface temperatures from two infrared window measurements with different absorption. J. Geophys. Res. 80, 5113–5117.
Menenti, M., Malamiri, H.G., Shang, H., Alfieri, S.M., Maffei, C., Jia, L., 2016. Observing the response of terrestrial vegetation to climate variability across a range of time scales by time series analysis of land surface temperature. In: Ban, Y. (Ed.), Multitemporal Remote Sensing. Remote Sensing and Digital Image Processing, 20, pp. 277–315.
Metz, M., Rocchini, D., Neteler, M., 2014. Surface temperatures at the continental scale: tracking changes with remote sensing at unprecedented detail. Remote Sens. 6, 3822–3840.
Metz, M., Andreo, V., Neteler, M., 2017. A new fully gap-free time series of land surface temperature from MODIS LST data. Remote Sens. 9, 1333.
Mo, Y., Xu, Y., Liu, Y., Xin, Y., Zhu, S., 2023. Comparison of gap-filling methods for producing all-weather daily remotely sensed near-surface air temperature. Remote Sens. Environ. 296, 113732.
Moffat, A.M., Papale, D., Reichstein, M., Hollinger, D.Y., Richardson, A.D., Barr, A.G., Beckstein, C., Braswell, B.H., Churkina, G., Desai, A.R., et al., 2007. Comprehensive

comparison of gap-filling techniques for eddy covariance net carbon fluxes. Agric. For. Meteorol. 147, 209–232.
Neteler, M., Roiz, D., Rocchini, D., Castellani, C., Rizzoli, A., 2011. Terra and Aqua satellites track tiger mosquito invasion: modelling the potential distribution of *Aedes albopictus* in north-eastern Italy. Int. J. Health Geogr. 10.
Pan, X., Wang, Z., Liu, S., Yang, Z., Guluzade, R., Liu, Y., Yuan, J., Yang, Y., 2024. The impact of clear-sky biases of land surface temperature on monthly evapotranspiration estimation. Int. J. Appl. Earth Obs. Geoinf. 129, 103811.
Pasotti, L., Maroli, M., Giannetto, S., Brianti, E., 2006. Agrometeorology and models for the parasite cycle forecast. Parassitologia 48.
Phiri, D., Simwanda, M., Salekin, S., Nyirenda, V., Murayama, Y., Ranagalage, M., 2020. Sentinel-2 data for land cover/use mapping: a review. Remote Sens. 12, 2291.
Piao, J., Chen, W., Wei, K., Cai, Q., Zhu, X., Du, Z., 2023. Increased sandstorm frequency in North China in 2023: climate change reflection on the Mongolian plateau. The Innovation 4, 100497.
Pouriyeh, A., Lotfi, F.H., Pirasteh, S., 2021. Vulnerability assessment and modelling of urban growth using data envelopment analysis. J. Indian Soc. Remote Sens. 49, 259–273.
Przeździecki, K., Zawadzki, J.J., Urbaniak, M., Ziemblińska, K., Miatkowski, Z., 2023. Using temporal variability of land surface temperature and normalized vegetation index to estimate soil moisture condition on forest areas by means of remote sensing. Ecol. Indic. 148, 110088.
Rodrigues, P.C., Mahmoudvand, R., 2018. The benefits of multivariate singular spectrum analysis over the univariate version. J. Frankl. Inst. 355, 544–564.
Samson Udama Eneche, P., Atun, F., Zeng, Y., Pfeffer, K., 2024. Robust drivers of urban land surface temperature dynamics across diverse landscape characters: an augmented systematic literature review. Ecol. Indic. 163, 112056.
Sarafanov, M., Kazakov, E., Nikitin, N.O., Kalyuzhnaya, A.V., 2020. A machine learning approach for remote sensing data gap-filling with open-source implementation: an example regarding land surface temperature, surface albedo and NDVI. Remote Sens. 12, 3865.
Schneider, P., Hook, S.J., 2010. Space observations of inland water bodies show rapid surface warming since 1985. Geophys. Res. Lett. 37.
Seitola, T., Silen, J., Järvinen, H., 2015. Randomised multichannel singular spectrum analysis of the 20th century climate data. Tellus A: Dyn. Meteorol. Oceanogr. 83, 28876.
Shawky, M., Ahmed, M.R., Ghaderpour, E., Gupta, A., Achari, G., Dewan, A., Hassan, Q. K., 2023. Remote sensing-derived land surface temperature trends over South Asia. Ecol. Inform. 74, 101969.
Siabi, N., Sanaeinejad, S., Ghahraman, B., 2022. Effective method for filling gaps in time series of environmental remote sensing data: an example on evapotranspiration and land surface temperature images. Comput. Electron. Agric. 193, 106619.
Simpson, J.J., Gobat, J.I., 1996. Improved cloud detection for daytime AVHRR scenes over land. Remote Sens. Environ. 55, 21–49.
Song, Z., Yang, H., Huang, X., Yu, W., Huang, J., Ma, M., 2021. The spatiotemporal pattern and influencing factors of land surface temperature change in China from 2003 to 2019. Int. J. Appl. Earth Obs. Geoinf. 104, 102537.
Song, P., Zhao, T., Zhang, Y., He, Q., 2023. Conversion of satellite passive microwave signals to land surface "skin" temperature for extremely dry deserts. Remote Sens. Environ. 299, 113857.
Stowe, L., McClain, E., Carey, R., Pellegrino, P., Gutman, G., Davis, P., Long, C., Hart, S., 1991. Global distribution of cloud cover derived from NOAA/AVHRR operational satellite data. Adv. Space Res. 11, 51–54.
Stubenrauch, C.J., Rossow, W.B., Kinne, S., Ackerman, S., Cesana, G., Chepfer, H., Di Girolamo, L., Getzewich, B., Guignard, A., Heidinger, A., Maddux, B.C., Menzel, W. P., Minnis, P., Pearl, C., Platnick, S., Poulsen, C., Riedi, J., Sun-Mack, S., Walther, A., Winker, D., Zeng, S., Zhao, G., 2013. Assessment of global cloud datasets from satellites: project and database initiated by the GEWEX radiation panel. Bull. Am. Meteorol. Soc. 94, 1031–1049.
Taheri Dehkordi, A., Valadan Zoej, M.J., Ghasemi, H., Ghaderpour, E., Hassan, Q.K., 2022. A new clustering method to generate training samples for supervised monitoring of long-term water surface dynamics using landsat data through Google earth engine. Sustainability 14, 8046.
Tahooni, A., Kakroodi, A., Kiavarz, M., 2023. Monitoring of land surface albedo and its impact on land surface temperature (lst) using time series of remote sensing data. Ecol. Inform. 75, 102118.
Tan, J., Che, T., Wang, J., Liang, J., Zhang, Y., Ren, Z., 2021. Reconstruction of the daily MODIS land surface temperature product using the two-step improved similar pixels method. Remote Sens. 13, 1671.
Tian, Y., Zhang, Y., 2022. A comprehensive survey on regularization strategies in machine learning. Information Fusion 80, 146–166.
Vautard, R., Ghil, M., 1989. Singular spectrum analysis in nonlinear dynamics, with applications to paleoclimatic time series. Phys. D: Nonlinear Phenom. 35, 395–424.
Vautard, R., Yiou, P., Ghil, M., 2013. Singular-spectrum analysis: a toolkit for short, noisy chaotic signals. Phys. D: Nonlinear Phenom. 58, 95–126.
Wan, Z., Dozier, J., 1996. A generalized split-window algorithm for retrieving land-surface temperature from space. IEEE Trans. Geosci. Remote Sens. 34, 892–905.
Wang, Y., Yi, G., Zhou, X., Zhang, T., Bie, X., Li, J., Ji, B., 2021. Spatial distribution and influencing factors on urban land surface temperature of twelve megacities in China from 2000 to 2017. Ecol. Indic. 125, 107533.
Weinberg, M.D., Petersen, M.S., 2021. Using multichannel singular spectrum analysis to study galaxy dynamics. Mon. Not. R. Astron. Soc. 501, 5408–5423.
Weng, Q., 2009. Thermal infrared remote sensing for urban climate and environmental studies: methods, applications, and trends. ISPRS J. Photogramm. Remote Sens. 64, 335–344.
Xian, G., Shi, H., Auch, R., Gallo, K., Zhou, Q., Wu, Z., Kolian, M., 2021. The effects of urban land cover dynamics on urban heat island intensity and temporal trends. GISci. Remote Sens. 58, 501–515.
Xiang, Y., Ye, Y., Peng, C., Teng, M., Zhou, Z., 2022. Seasonal variations for combined effects of landscape metrics on land surface temperature (LST) and aerosol optical depth (AOD). Ecol. Indic. 138, 108810.
Xiao, Y., Zhao, W., Ma, M., He, K., 2021. Gap-free LST generation for MODIS/Terra LST product using a random forest-based reconstruction method. Remote Sens. 13, 2828.
Xing, Z., Li, Z.L., Duan, S.B., Liu, X., Zheng, X., Leng, P., Gao, M., Zhang, X., Shang, G., 2021. Estimation of daily mean land surface temperature at global scale using pairs of daytime and nighttime MODIS instantaneous observations. ISPRS J. Photogramm. Remote Sens. 178, 51–67.
Xu, Y., Shen, Y., 2013. Reconstruction of the land surface temperature time series using harmonic analysis. Comput. Geosci. 61, 126–132.
Yan, D., Yu, H., Xiang, Q., Xu, X., 2023. Spatiotemporal patterns of land surface temperature and their response to land cover change: a case study in Sichuan Basin. Egypt. J. Remote Sens. Space Sci. 26, 1080–1089.
Yan, W., Jiang, J., He, L., Zhao, W., Nair, R., Wang, X., Xiong, Y., 2024. Correcting land surface temperature from thermal imager by considering heterogeneous emissivity. Int. J. Appl. Earth Obs. Geoinf. 129, 103824.
Yao, R., Wang, L., Huang, X., Sun, L., Chen, R., Wu, X., Zhang, W., Niu, Z., 2021. A robust method for filling the gaps in MODIS and VIIRS land surface temperature data. IEEE Trans. Geosci. Remote Sens. 59, 10738–10752.
Yiou, P., Sornette, D., Ghil, M., 2000. Data-adaptive wavelets and multi-scale singular-spectrum analysis. Phys. D: Nonlinear Phenom. 142, 254–290.
Yoo, C., Im, J., Park, S., Quackenbush, L.J., 2018. Estimation of daily maximum and minimum air temperatures in urban landscapes using MODIS time series satellite data. ISPRS J. Photogramm. Remote Sens. 137, 149–162.
Zamani Losgedaragh, S., Rahimzadegan, M., 2018. Evaluation of SEBS, SEBAL, and METRIC models in estimation of the evaporation from the freshwater lakes (case study: Amirkabir dam, Iran). J. Hydrol. 561, 523–531.
Zhang, C., Li, W., Travis, D., 2007. Gaps-fill of SLC-off Landsat ETM+ satellite image using a geostatistical approach. Int. J. Remote Sens. 28, 5103–5122.
Zhang, X., Zhou, J., Liang, S., Chai, L., Wang, D., Liu, J., 2020. Estimation of 1-km all-weather remotely sensed land surface temperature based on reconstructed spatial-seamless satellite passive microwave brightness temperature and thermal infrared data. ISPRS J. Photogramm. Remote Sens. 167, 321–344.
Zhou, J., Jia, L., Menenti, M., Liu, X., 2021. Optimal estimate of global biome—specific parameter settings to reconstruct NDVI time series with the harmonic ANalysis of time series (HANTS) method. Remote Sens. 13, 4251.
Zhou, J., Menenti, M., Jia, L., Gao, B., Zhao, F., Cui, Y., Xiong, X., Liu, X., Li, D., 2023. A scalable software package for time series reconstruction of remote sensing datasets on the google earth engine platform. Int. J. Digit. Earth 16, 988–1007.
Zhu, W., Lű, A., Jia, S., 2013. Estimation of daily maximum and minimum air temperature using MODIS land surface temperature products. Remote Sens. Environ. 130, 62–73.
Zhu, X., Duan, S.B., Li, Z.L., Wu, P., Wu, H., Zhao, W., Qian, Y., 2022. Reconstruction of land surface temperature under cloudy conditions from landsat 8 data using annual temperature cycle model. Remote Sens. Environ. 281, 113261.